Ion-driven fast ignition: reducing heavy-ion fusion driver energy and cost, simplifying chamber design, target fab, tritium fueling, and power conversion

---

White paper for the conference on Innovative Confinement Concepts
Princeton Plasma Physics Laboratory
April 6-9, 1998
G. Logan, D. Callahan-Miller, J. Perkins, G. Caporaso, M. Tabak, R. Moir, W. Meier
Lawrence Livermore National Laboratory*, Livermore, CA 94550
Roger Bangerter, Ed Lee
Lawrence Berkeley National Laboratory, Berkeley, CA

Contents:

Abstract

Ion fast ignition, like laser fast ignition, can potentially reduce driver energy for high target gain by an order of magnitude, while reducing fuel capsule implosion velocity, convergence ratio, and required precisions in target fabrication and illumination symmetry, all of which should further improve and simplify IFE power plants. From fast-ignition target requirements, we determine requirements for ion beam acceleration, pulse-compression, and final focus for advanced accelerators that must be developed for much shorter pulses and higher voltage gradients than today's accelerators, to deliver the petawatt peak powers and small focal spots (~100 μm) required. Although such peak powers and small focal spots are available today with lasers, development of such advanced accelerators is motivated by the greater likely efficiency of deep ion penetration and deposition into pre- compressed 1000x liquid density DT cores. Ion ignitor beam parameters for acceleration, pulse compression, and final focus are estimated for two examples based on a Dielectric Wall Accelerator; (1) a small target with ρr~2 g/cm^2 for a small demo/pilot plant producing ~40 MJ of fusion yield per target, and (2) a large target with ρr~10 g/cm^2 producing ~1 GJ yield for multi-unit electricity/hydrogen plants, allowing internal T-breeding with low T/D ratios, >75 % of the total fusion yield captured for plasma direct conversion, and simple liquid-protected chambers with gravity clearing. Key enabling development needs for ion fast ignition are found to be (1) "Close- coupled" target designs for single-ended illumination of both compressor and ignitor beams; (2) Development of high gradient (>25 MV/m) linacs with high charge-state (q ~26) ion sources for short (~5 ns) accelerator output pulses; (3) Small mm-scale laser-driven plasma lens of ~10 MG fields to provide steep focusing angles close-in to the target (built-in as part of each target); (4) beam space charge-neutralization during *both* drift compression and final focus to target. Except for (1) and (2), these critical issues may be explored on existing heavy-ion storage ring accelerator facilities.

I. Introduction

Fast ignition (fast heating of DT cores *after* compression) reduces driver energy (by 10 X or more) by reducing the implosion velocity and energy for a given fuel compression ratio [1]. For any type of driver that can deliver the ignition energy fast enough, fast ignition increases the target gain compared to targets using fast implosions for central ignition, as long as the energy to heat the core after compression is comparable to or less than the slow compression energy, and as long as the coupling efficiency of the fast ignitor beam to heat the core is comparable to the overall efficiency of compressing the core (in terms of beam energy-to-DT-efficiency). The fast ignition energy after compression has to be supplied before the heated region of compressed fuel can dissasemble, in a time less than 20 to 100 picoseconds, hence the name. Ion driven fast ignition, compared to laser-driven fast ignition, has the advantage of direct (dE/dx) deposition of beam energy to the DT, eliminating inefficiencies for conversion into hot electrons, and direct ion heating also has a more favorable deposition profile, with the Bragg-peak in local ion energy deposition occuring near the end of an ion range that can reach deep inside a compressed DT core. The two-step fast ignition process using two different ion beams is depicted in Fig.1 for indirect-drive targets.

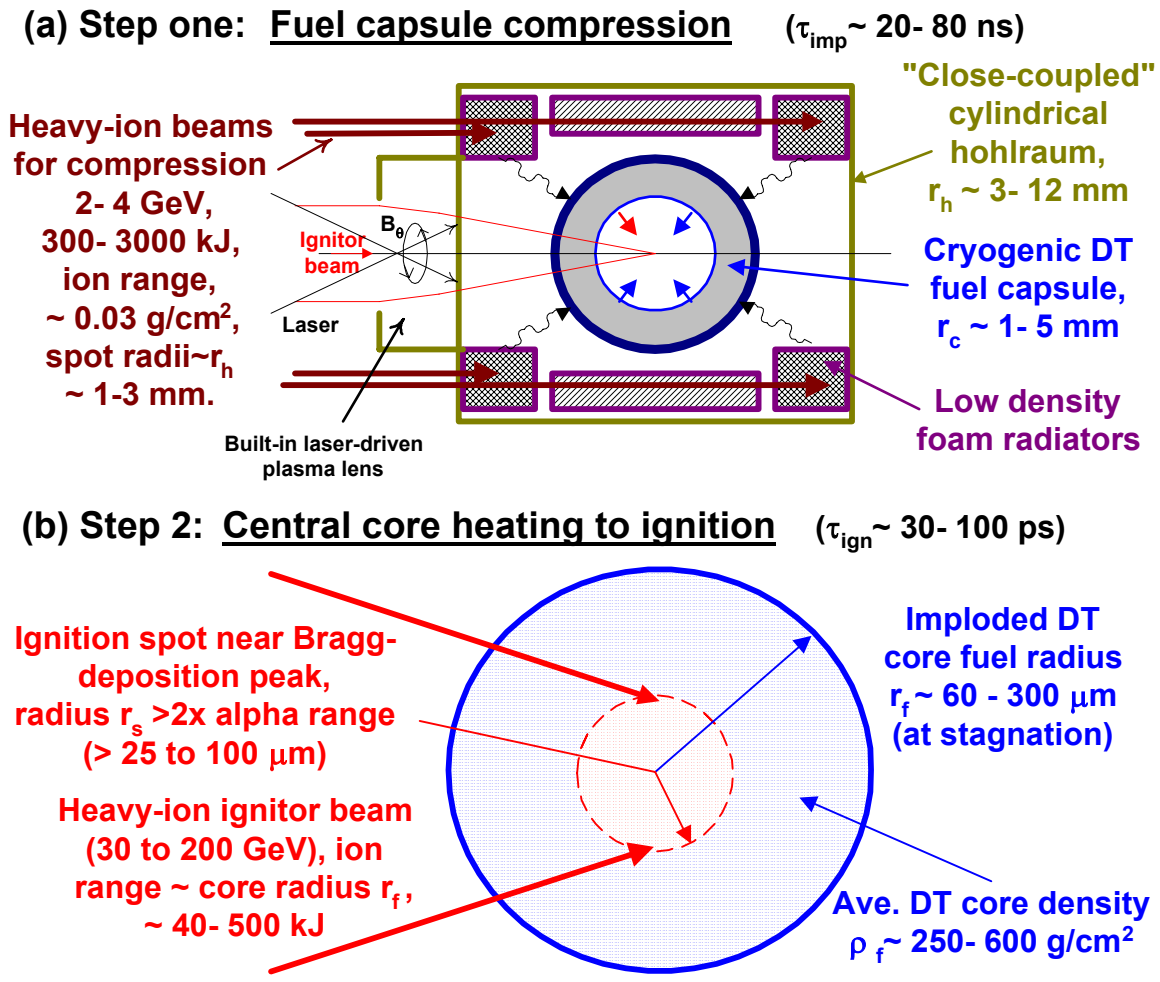

Fig. 1 : Ion fast ignition in two steps; capsule compression with long-pulse ion beams (a), followed by ignition of the imploded DT core [shown magnified] with a short pulse ion beam (b). Parameters range from smallest (left) to largest (right) power plant targets.

A wide range of possible target parameters is indicated in Fig. 1 to cover both small targets for a small IFE demo/pilot plant, and large targets for a large multi-unit hydrogen plant that will be discussed in more detail in Section II. The hohlraum shown in Fig. 1 has a cylindrical case just larger enough than the capsule radius to allow for the beam spot diameters traversing the distributed radiators, hence the name "close-coupled" hohlraum. We have just started such target designs at LLNL for conventional hot-spot ignition using distributed radiators with two sided beam illumination. With reduced symmetry and convergence ratio, we assume that such targets can be driven with beams coming from a single end for fast ignition. In general, range-shortening may require use of two different beam energies for the compression beams (Fig. 1a), as in the case of conventional hot-spot ignition targets with distributed radiators [2]. The fast ignitor ion beam (the dashed beam in the center of Fig. 1a) is also assumed to come from the same side as the compression beams. The ignitor beam is focused to the the capsule center by a laser-generated B_θ field just outside the hohlraum end cap. This laser-powered ignitor beam lens, built into each hohlraum, will be described later on in section III.

Laser-driven fast ignition would also be a two-step process as in Fig. 1, although the laser-beam parameters and target geometry would be different. Laser fast ignition is considered in a separate ICC white paper by Stevens, et. al., at this conference [3]. It is also possible in principle to achieve high gain by a combination of ions to compress the fuel capsule and a laser to ignite the compressed fuel, and vice versa. The idea of using ion beams to heat a DT target to ignition after compression was considered very early in the heavy-ion fusion program by Maschke [4], but heavy-ion target designs for conventional compression heating of a central hot spot was pursued instead, since the latter case allows lower peak driver beam powers and larger focal spots delivered to a target, closer to the anticipated capabilities thought to be achievable for heavy-ion accelerators. In Section II, we will in fact consider target designs for ion fast ignition which allow both larger focal spots and longer pulses on the target, to help relax the stringent accelerator requirements for the ignitor beam. For driver beams used to drive the capsule implosion for fuel compression, fast ignition allows lower fuel implosion velocity and kinetic/internal energy, which both reduces the energy for compression as well as lengthen the pulse allowed for the compressor beams. Despite the reduced fuel compression energy, fast ignition itself generally requires less driver energy than that required for the slow fuel compression, for either ion or laser drivers. Fast ignition would still result in more than 2x higher target gain than conventional targets, even if the fast ignition beam energy requirement became comparable to the compression beam energy.

Fast ignition R&D, either for laser or ion drivers, is motivated not just for the possibility of higher target gain for IFE, but also because it relaxes the most demanding target stability requirement of the standard approach to inertial fusion, namely, the formation of an hot, low density igniting hot spot in the center of a dense imploding fuel shell. The hot spot in the standard approach is inherently Rayleigh Taylor unstable, which sets stringent requirements for ignition; namely, high minimum implosion velocities which can be limited by plasma instabilities in the hohlraum or capsule-ablator plasma-beam interactions, a very demanding degree of drive symmetry on the capsule (either by x-rays in indirect-drive, or by laser light in direct drive), and fabrication of very smooth capsule abators with very smooth internal DT cryo layers to limit growth of hydrodynamic instabilities and associated mix of cold fuel and hot spot. In contrast, fast ignition allows complete mix in the DT core at stagnation, and subsequent ignition from an external ignitor beam is not very sensitive to the shape of the imploded DT core. For power plants, fast ignition with either laser or ions opens up more possibilites for IFE (Section IV), including use of tritium-depleted fuel with internal T-breeding [5], and the possibilty of aspherical targets driven with fewer beams from fewer directions, simplifying and expanding options for fusion chamber design.

Lasers with chirped-pulse amplification giving thousand-fold pulse compressions have been demonstrated to produce the short pulses, small focal spots and Petawatt peak powers approaching those required for fast ignition. In addition, high-intensity laser experiments at LLNL, ILE(Japan), and RAL(England) have demonstrated adequate hot electron energies and light-to-hot-electron conversion efficiencies for fast ignition. However, it is not yet known if light and hot electrons can channel deeply enough through a target's coronal plasma to heat a small portion of a 1000x liquid-density compressed DT core to ignition. On the other hand, accelerators do not yet exist which produce ion beams of sufficient peak power and beam quality for fast ignition, and so this paper addresses the advances in heavy-ion accelerator beam parameters that will be required to provide the fast ignitor beams as indicated in Fig.1.

To compress ion bunches to shorter lengths, a coherent velocity spread ("tilt") is imposed by tailoring the accelerator voltage pulses to make the beam tail go faster to catch up with the beam head. Part of the beam length compression can be accomplished during acceleration within the accelerator, with additional pulse compression in a drift space between the output of the accelerator and the target. Thus, velocity tilt plays the analogous role for ion beam pulse compression as frequency chirp does with lasers using a pair of diffraction gratings to cause rays of different color to overlap by taking different pathlengths to the target. Picosecond ion bunches have been demonstrated using the principle of velocity tilt at very low ion beam currents where space charge efects are negligible [5], but the challenge is to extend this technique to kiloamperes of beam current. Aside from space charge effects, Liouville's theorem preserves the product of ion bunch length and the random (therma)l velocity spread, so that any initial thermal velocity spread in a long ion bunch also constrains the maximum achievable bunch length compression ratio. These limits will be examined shortly in Section III.

Accordingly, it is the accelerator and final focusing physics, not the target coupling physics, that poses the main challenge to ion-driven fast ignition. As the mainline heavy-ion fusion program is concentrating on induction linacs, (which in any case is assumed will supply the main energy of compression in any kind of heavy-ion target), the purpose of this ICC white paper is to explore possible new features and characteristic parameters that advanced linacs would need to meet the stringent beam quality and pulse compression (sufficiently low longitudinal and transverse thermal spread) for an ion ignitor beam. For concreteness, we will use the Dielectric-Wall Accelerator (DWA) concept [6] to evaluate two examples of fast ignition for a small demo/pilot plant and for a larger multi-unit IFE plant, although the same general beam requirements for the fast ignitor beam could also apply to other advanced accelerators capable of similar high voltage gradients and multi-kA beam currents.

As the concepts described in this white paper are quite new, the models are very rudimentary and have not yet been carefully verified in detail. However, in keeping with the spirit of the Innovative Confinements Concepts meeting, we have tried to illustrate some possible impacts of ion driven fast ignition by concrete examples, with no attempt to be complete or optimum. The aim of this white paper is to stimulate thinking and debate and to define the required R&D, hopefully leading to more detailed target designs, particle beam simulations, small-scale experimental tests of the most novel accelerator elements, and to tests of novel focusing optics using exisitng heavy-ion storage ring facilities in Germany, Russia, and Japan (Section V).

II. Target requirements for ion fast ignition

There are many different conceivable types of fast ignitor target geometries, howerver, the one shown in Fig. 1 is chosen for this white paper because it is the simplest to describe with a simple model. One can expect even better optimized designs in the future. We are currently developing a "target road map" in ρ versus ρr space for ion-driven fast ignition, to give accelerators designers a way to optimize choices of accelerator and target parameters together. When that road map is finished, the "best" accelerator (either linac or synchrotron) can be optimized. However, any type of accelerator will likely need some new design features to meet stringent fast ignition pulse requirements that will be more challenging than conventional HIF anywhere in the ρ vs ρr space. In the following, we will present a very simple analytical model for the compression and fast ignition of spherical ion-driven fast ignition capsules as depicted in Fig. 1.

To check the fast-ignition part (Fig.1b) of the model, we recently completed a series of 2-D target burn calculations for ion-driven fast ignition which are listed in Table 1, along with the predictions of the simple model. The model is then used to extrapolate requirements for compression and fast ignition to a smaller target for an IFE pilot plant, and for a larger target for a hydrogen/electric multi-unit plant. The 2-D burn calculations start with a pre-compressed sphere of 50% D- 50-% T having a given density ρ_f and ρr_f product value in each case. The 2-D burn calculations determine the minimum ion ignition energy and corresponding fusion yield for the chosen ion range and spot size in each case. Since heavy-ions slow down by dE/dx electron drag with minimal side-scatter, virtually 100 % of the ion ignitor beam energy gets depositied along the ion path in the DT, with a Bragg peak near the end of the ion range. A single ignitor beam is assumed, although in general several ion ignitor beams could be also be used. In the 2-D calculations, the ignitor beam is assumed to have a Gaussian radial profile, with r_s = FWHM / 2 .

Compression

The ion beam energy requirement for the compression beam system is estimated using an overall efficiency η_c of ion beam energy incident onto the distributed target radiators shown in Fig. 1a, to the compressed DT internal energy (product of hohlraum-coupling efficiency x hydro-compression efficiencies):

$$\eta_c := 0.07$$

[In a MathCAD document like this one, an " := " means the same thing as " = ".] This value of compression efficiency is extrapolated from previous distributed radiator designs [2], taking credit for expected improvements from current work to shrink the holraum case closer around the capsule (hence the name "close-coupled hohlraum"). For reference, the NIF indirect-drive target has a corresponding value of η_c ~ 1.7 %, and recent 2-D distributed radiator designs for conventional ignition by Tabak and Callahan [2] achieves η_c ~ 3.5 %, a factor of two higher than NIF due to the fact that heavy-ion hohlraums have less radiation losses (no laser entrance holes). As a reasonable goal, we take fast ignition fuel compression assuming η_c of 7 %, another factor of two higher, to credit the expectation that reduced symmetry requirements for fast ignition will allow a more compact hohlraum with a lower case-to-capsule radius, and hence lower hohlraum wall losses and radiator mass.

We assume a minimum implosion adiabat value that might result from imperfect pulse shaping to be

$$\alpha := 1.25$$

The corresponding specific energy in the compressed DT is then

$$\varepsilon_c(\rho_f, \alpha) := 2.4 \cdot 10^5 \cdot \alpha \cdot (\rho_f)^{0.667} \quad \text{(J/g),} \quad \text{Eq.1}$$

and the corresponding compression beam energy required is estimated by:

$$E_c(\rho r_f, \rho_f, \alpha, \eta_c) := \frac{4}{3} \cdot \pi \cdot \left(\frac{\rho r_f}{\rho_f}\right)^3 \cdot \rho_f \cdot \frac{\varepsilon_c(\rho_f, \alpha)}{\eta_c} \quad \text{(J).} \quad \text{Eq. 2}$$

[Here density is in grams per cm^3, radii in cm, so ρr products are in grams per cm^2.] Note for a given ρr_f product, that E_c scales as 1/ $\rho^{1.33}$, so that compression energy for a given ρr_f decreases with increasing ρ_f . However, keep in mind that larger ρ_f also makes symmetry more stringent, and raises the minimum implosion velocity v_{imp}, which can be scaled roughly from

$$v_{imp}(\rho_f) := 3.6 \cdot 10^7 \cdot \left(\frac{\rho_f}{1200}\right)^{0.333} \quad \text{(At end of drive pulse, cm/s)} \quad \text{Eq. 3}$$

For a rough estimate of the FWHM of the peak-power pulse width for the compression beams, one can use a characteristic value

$$\tau_{peak}(r_c, \rho_f) := \frac{1.2 \cdot r_c}{v_{imp}(\rho_f)} \quad \text{(s).} \quad \text{Eq. 4}$$

Using a properly shaped pulse to achieve a low implosion adiabat α of 1.5, the overall compression beam pulse width, including the foot, would be about 3 to 4 times this characteristic τ_{peak}.

Fast Ignition

The specific deposited energy per gram ε_i required for the ignitor beam to heat DT fuel up from some initial temperature T_s at stagnation to a minimum ignition temperature (T_{ig}) sufficient to launch a propagating alpha-driven burn wave from the beam-heated region, depends both on the ρr of the beam-heated region (ρr_s) relative to a fusion alpha range ~0.3 g/cm^2, as well as on the ratio χ of the ignitor heating pulse width τ_i to the characteristic expansion time r_s/C_s of the beam-heated region :

$$\chi(r_s, \tau_i, T_{ig}) := \tau_i \cdot 10^8 \cdot \sqrt{\frac{T_{ig}}{10}} \cdot r_s^{-1} \quad \text{Eq. 5}$$

When χ <<1, the deposited ignitor beam energy has to provide only the minimum internal energy [3nTV] to heat the DT to T_{ig} isochorically, but for longer ion pulses with χ comparable to or larger than unity (which we will consider here), the deposited ignitor beam energy has to provide both the internal energy of heating up the DT temperature in the vicinity of the ion Bragg deposition-peak , plus the PdV hydro expansion work expended by the DT hot "bubble" when it is heated to a pressure greater than the surrounding cold DT fuel.

The minimum ignition temperature generally decreases with larger ρr_s hot spots, which we crudely model here as

$$T_{ig}(\rho_f, r_s) := 4.5 \cdot \left(\frac{0.3 + \rho_f \cdot r_s}{\rho_f \cdot r_s} \right)^3 \qquad \text{(keV)} \qquad \text{Eq. 6}$$

This a pessimistic model to take some account of our neglect of thermal conduction losses from the hot spot. At the minimum hot spot size ρr_s = 0.3 g/cm^2, Eq. 6 gives T_{ig} = 36 keV; at ρr_s = 0.6, T_{ig} = 15 keV, and at very large ρr_s>>0.3, a lower bound to the ideal T_{ig} = 4.5 keV. At large ρr, self-trapping of bremsstrahlung can be significant. To take a very rough account of the scaling of the added hot spot expansion energy for finite χ_o , we assume a scaling of required specific energy deposition in joules per gram to be

$$\varepsilon_i(\rho_f, r_s, \chi_o) := 7.67 \cdot 10^7 \cdot T_{ig}(\rho_f, r_s) \cdot \left(\frac{3}{2} + \chi_o^{\,3} \right) \qquad \text{(J/g)} \qquad \text{Eq. 7}$$

where we have neglected any initial stagnation temperature T_s compared to T_{ig}. For χ << 1 and for T_{ig} = 10 keV, Eq. 7 gives the usual ε_i ~ 1.15x10^9 J/g. The expansion term scaling in Eq. 7 is taken to be χ3 to model a roughly spherical DT hot "bubble" expansion in the vicinity of the Bragg peak. Now, considering the ignitor beam geometry as Fig. 1b, and recognizing that the ion Bragg deposition peak would be near the end of the chosen range R (g/cm^2) where the ignitor beam spot radius is r_s, we can estimate the effective total mass of DT heated by the ignitor beam to be

$$M_{ig}(r_s, \chi_o, R) := \frac{\pi \cdot r_s^{\,2} \cdot R}{1 + \chi_o^{\,2}} \qquad \text{(g)} \qquad \text{Eq. 8}$$

where we have included a cylindrical-like expansion factor (1+ χ^2) to account for DT mass reduction within the ion beam channel due to the hot DT "bubble" expansion beyond the ignitor beam radius. (DT expansion along the beam channel doesn't escape the beam because constant range ions can "chase" the DT expanding in the beam direction). With these assumptions, the required ignitor beam deposition energy is:

$$E_i(\rho_f, r_s, \chi_o, R) := M_{ig}(r_s, \chi_o, R) \cdot \varepsilon_i(\rho_f, r_s, \chi_o) \qquad \text{(J)} \qquad \text{Eq. 9}$$

For a given χ_o, this ignitor energy E_i has to be delivered in a time

$$\tau_{ig}(\rho_f, r_s, \chi_o) := \frac{\chi_o \cdot r_s}{10^8 \cdot \sqrt{\frac{T_{ig}(\rho_f, r_s)}{10}}} \quad \text{(s).} \qquad \text{Eq. 10}$$

Fusion yield

For ion fast ignition starting with a stagnated DT core, the 2-D burn calculations indicate that the effective core ρr_f is reduced about a factor of two below its initial value by the time an alpha burn wave starts propagating from the beam heated zone; thus we use a factor of 12 instead of 6 in the normal expression for burnup fraction:

$$f_b(\rho r_f, X) := \frac{\rho r_f}{\rho r_f + 12 \cdot \left[\frac{1 + 0.5 \cdot X}{X \cdot (1 - X)} \cdot \frac{1}{5}\right]} \qquad \text{Eq. 11}$$

Future optimization may find that the optimal timing for the ignitor heating pulse is just before the stagnation of the implosion. The factor in square brackets in Eq. 11 contains the burnup dependence on the average tritium fraction in the fuel $X = n_T / (n_D + n_T)$. For X = 0.5 (50% D, 50% T mixture), the term in square brackets is unity. For X < 0.1, Atzehni has shown that D-D side reactions result in net tritum breeding *in-situ*, for large ρr targets ignited with a small X = 0.5 spark-plug region, which results in very high burn temperatures > 50 keV, where D-D side reactions are vigorous. For such a target, the DT layer of the capsule in Fig. 1a would consist mostly of a tritium-lean outer layer, with a thin X=0.5 DT-rich inner layer, such that the compressed core of Fig. 1b would end up with X=0.5 inside the ignitor beam radius r_s in the core, with an average X<0.1 in the rest of the core. For ρr ~ 10 g/cm^2 and X = 0.1, the marginal tritium- self-sufficiency point, Eq. 11 predicts a burnup fraction of 26 %, compared to 45% at the same ρr with an average X=0.5. Using Eq. 11 and a specific fusion DT energy release of 3.54 x 10^{11} J per gram of fuel burned, the fusion yield can be estimated by

$$Y(\rho r_f, \rho_f, X) := 3.54 \cdot 10^{11} \cdot f_b(\rho r_f, X) \cdot \frac{4}{3} \cdot \pi \cdot \left(\frac{\rho r_f}{\rho_f}\right)^3 \cdot \rho_f \quad \text{(J),} \qquad \text{Eq. 12}$$

Note that the actual burnup fraction and total fusion yield is underestimated by Eq. 11 and 12, repectively, since the D-D side reactions are neglected in both for simplicity. This is a significant underestimate for X = 0.1, since at the tritium self-sufficiency point, there are two D-D side reaction for every D-T reaction, to balance tritium production and burning. Using Eq. 12 for the fusion yield, the resultant target energy gain is

$$G(\rho r_f, \rho_f, X, r_s, \chi_o, \alpha, \eta_c, R) := \frac{Y(\rho r_f, \rho_f, X)}{E_c(\rho r_f, \rho_f, \alpha, \eta_c) + E_i(\rho_f, r_s, \chi_o, R)} \qquad \text{Eq. 13}$$

Note that the overall beam-to-DT coupling efficiency η_c is included in the compression energy E_c in Eq. 13, while the ignitor beam coupling efficiency is virtually 100 % in the ignition energy term E_i, as long as the ion ignitor range is significantly less than the fuel ball *diameter*, the ignitor beam radius is at least a factor of two smaller than the compressed core radius, and the ignitor beam pointing error is about the same or less than the beam radius.

Comparison of model with 2-D burn calculations

We can now compare the predictions of the above simple model for nine 2-D burn calculations, and then apply the model to estimate one additional case (10) for which we have not yet done a 2-D burn calculation. Cases 9 and 10 represent a small and large target for our two extreme power plant examples: a smallest ρr target such that the product of driver efficiency and target gain ηG is still >40 (assuming a driver wall-plug efficiency η_d = 20% for the weighted-average efficiency of both compression and ignition beams, that condition requires a target gain G > 200), and a large ρr = 10 g/cm^2 target for a large hydrogen plant to get self-sufficient *in-situ* tritium breeding with X=0.1 fuel mix, and to capture >75% of the fusion yield in charged particles for plasma direct conversion [8]. [In the latter case, there would also be few-cm thick target sabot-shell surrounding the hohlraum (not shown in Fig. 1), to both lower the average plasma temperature to a few eV, and to absorb the target x-ray output. The sabot material would become part of the plasma working fluid for direct conversion].

The following array elements for cases denoted by the subscript numbers one through nine are assigned to the input values used in the 2-D burn calculations; case 10 is for the big target. Table 1 below summares the results of the comparisons of cases 1 to 9, and the model predictions for case 10.

For $j := 1 .. 10$ different values of stagnation ρr_f and ρ_f values given by :

$\rho rf_1 := 4.3$ $\rho rf_2 := 3$ $\rho rf_3 := 3$ $\rho rf_4 := 3$ $\rho rf_5 := 2.5$
$\rho rf_6 := 4$ $\rho rf_7 := 4$ $\rho rf_8 := 4$ $\rho rf_9 := 2$ $\rho rf_{10} := 10$
Compressed fuel (ρr_f) values (g/cm2)

$\rho f_1 := 375$ $\rho f_2 := 128$ $\rho f_3 := 128$ $\rho f_4 := 128$ $\rho f_5 := 128$
$\rho f_6 := 256$ $\rho f_7 := 256$ $\rho f_8 := 256$ $\rho f_9 := 200$ $\rho f_{10} := 600$
Compressed fuel densities (ρ_f) values (g/cm3)

$\tau ig_1 := 35$ $\tau ig_2 := 234$ $\tau ig_3 := 117$ $\tau ig_4 := 2.3$ $\tau ig_5 := 234$
$\tau ig_6 := 156$ $\tau ig_7 := 50$ $\tau ig_8 := 50$ $\tau ig_9 := 30$ $\tau ig_{10} := 100$
Ignitor pulse width (τ) values (ps)

$rs2_1 := 22.5$ $rs2_2 := 100$ $rs2_3 := 100$ $rs2_4 := 100$ $rs2_5 := 100$
$rs2_6 := 78$ $rs2_7 := 78$ $rs2_8 := 78$ $rs2_9 := 25$ $rs2_{10} := 50$
Ignitor beam spot radius (rs2) values (μm). rs2 denotes the secondary spot in a two-lens scheme.

$Tig_{mo_j} := T_{ig}\left(\rho f_j, rs2_j \cdot 10^{-4}\right)$ Model predictions for the ignition temperature (keV)

$\chi o_j := \chi\left(rs2_j \cdot 10^{-4}, \tau ig_j \cdot 10^{-12}, Tig_{mo_j}\right)$ Ratios of ignitor pulse widths to hot spot expansion times (Model). Typical values range between 0.5 and 2.

$R_1 := 2.5$ $R_2 := 3.2$ $R_3 := 3.2$ $R_4 := 3.2$ $R_5 := 4.5$ Ignitor ion ranges (R) values (g/cm^2)

$R_6 := 4$ $R_7 := 2.5$ $R_8 := 1.4$ $R_9 := 1$ $R_{10} := 10$

$Ei2d_1 := 56$ $Ei2d_2 := 1300$ $Ei2d_3 := 870$ $Ei2d_4 := 720$ $Ei2d_5 := 1300$ Ignitor beam energies (kJ) (2D-calcs.)

$Ei2d_6 := 620$ $Ei2d_7 := 310$ $Ei2d_8 := 220$ $Ei2d_9 := 68$ $Ei2d_{10} := 0$

$Eimo_j := Ei\left(\rho f_j, rs2_j \cdot 10^{-4}, \chi o_j, R_j\right) \cdot 10^{-3}$ Model predictions for the ignitor beam energy (kJ).

$Ecmo_j := Ec\left(\rho rf_j, \rho f_j, \alpha, \eta_c\right) \cdot 10^{-3}$ Model predictions for compression beam energy (kJ).

$Y2d_1 := 224$ $Y2d_2 := 430$ $Y2d_3 := 497$ $Y2d_4 := 576$ $Y2d_5 := 460$ Fusion yields (MJ)-2D calcs.

$Y2d_6 := 320$ $Y2d_7 := 371$ $Y2d_8 := 376$ $Y2d_9 := 43$ $Y2d_{10} := 0$

$X_j := 0.5$ $X_{10} := 0.1$ Average tritium fractions n_T / (n_D + n_T)

$Ymo_j := Y\left(\rho rf_j, \rho f_j, X_j\right) \cdot 10^{-6}$ Model predictions for the fusion yield (MJ).

$Gmo_j := G\left(\rho rf_j, \rho f_j, X_j, rs2_j \cdot 10^{-4}, \chi o_j, \alpha, \eta_c, R_j\right)$ Model predictions for the target gain

Table 1 Summary of 2-D burn ion fast ignition burn calculations (Cases 1 to 9) with the simple fast ignition model. Case 9 is the model prediction for the smallest ρr target which gives $\eta_d G$ > 40 for a small pilot plant; Case 10 is for a large target capable of self-sufficient in-situ tritium breeding, and capturing >75% fusion yield for plasma direct conversion.

Case	ρr_f	Density	Ignitor pulse	Ignitor spot	Ignitor range	Ignitor energy (2-D)	Ignitor energy (model)	Compres. beam (model)	Fusion yield (2-D)	Fusion yield (model)	Target gain (model)
$j =$	$\rho rf_j =$	$\rho f_j =$	$\tau ig_j =$	$rs2_j =$	$R_j =$	$Ei2d_j =$	$Eimo_j =$	$Ecmo_j =$	$Y2d_j =$	$Ymo_j =$	$Gmo_j =$
1	4.3	375	35	22.5	2.5	56	55	529	224	221	379
2	3	128	234	100	3.2	1300	1329	753	430	489	235
3	3	128	117	100	3.2	870	831	753	497	489	309
4	3	128	2.3	100	3.2	720	978	753	576	489	282
5	2.5	128	234	100	4.5	1300	1869	436	460	244	106
6	4	256	156	78	4	620	648	708	320	362	267
7	4	256	50	78	2.5	310	323	708	371	362	351
8	4	256	50	78	1.4	220	181	708	376	362	407
9	2	200	30	25	1	68	44	123	43	42	253
10	10	600	100	50	10	0	553	3555	0	1084	264
	g/cm^2	g/cm^3	ps	μm	g/cm^2	kJ	kJ	kJ	MJ	MJ	

Comparing the model predictions with the 2-D calculations for ignition energy and fusion yield for cases 1 to 9 in Table 1 shows adequate agreement for present purposes (within + or - 33% or better) except for case 5. However, Case 5 is not expected to agree, because it was the only case that had a 40 micron-thick heavy-metal tamper around the compressed core in the 2-D calculation. The large over-prediction of ignition energy and under-prediction of fusion yield for case 5 by the model, which does not assume any metal tamper, in fact reflects the expected benefits of adding a metal tamper layer. One notes from Table 1 that Case 9, despite the disadvantage of small ρr_f =2, and Case 10, despite the disadvantage of reduced reactivity due to tritium lean fuel mix, both achieve a target gain well over 200. This means that both the compressor beam and ignitior beam accelerator could be allowed to take advantage of lower efficiency technology, if it were cheaper, and still achieve a very low recirculating power for the driver.

III. Accelerator requirements for ion fast ignition

Compression Beam Requirements

The pulse length for the compression beams with fast ignition targets can be longer than otherwise would be required for conventional fast igntion. Longer pulse length requirements may reduce the cost per joule of inductions linacs or storage rings used to provide the compression energy, and also reduces the required velocity tilt and drift bunch compression ratio after acceleration, relaxing the maximum longitudinal velovcity spread $\delta p_z/p_z$ required for focusing to the target. The inital capsule radius and aspect ratio are optimization variables for future target designs, but for now we'll take initial capsule radii of

$r_{c_9} := 0.1$ (cm), and $r_{c_{10}} := 0.5$ (cm)

(Small power plant case) (Large power plant case).

corresponding to the Case 9 and Case 10 targets, respectively. [The smaller capsule would have a relatively-thicker fuel layer (smaller capsule aspect ratio) than the larger target, since the smaller target requires lower compressed density and convergence ratio]. and] During the implosion driven by a shaped-pulse x-ray drive, the capsule accelerates up to a maximum implosion velocity v_{imp} which must be high enough to provide both the DT shell kinetic energy and compression energy (Fermi-energy x α) at the point of ignition. For fast ignition, there is no hot spot velocity requirement at ignition, although that is another optimization variable to explore in future designs. The characteristic FWHM of the final peak of a shaped compression pulse, estimated by Eq. 4, is about 3-4 times less than the total compression drive pulse width. However, the most demanding compression accelerator requirement is the peak requirement, set by the peak FWHM time:

$\tau_{peak}\left(r_{c_9}, \rho f_9\right) = 6.1 \times 10^{-9}$ (s), and $\tau_{peak}\left(r_{c_{10}}, \rho f_{10}\right) = 2.1 \times 10^{-8}$ (s)

(Small pilot plant case) (Large power plant case).

The total pulse widths for the shaped pulses would be ~ 4 times these peak pulse widths.

The corresponding implosion velocities are:

$v_{imp}(\rho f_9) = 2 \times 10^7$ (cm/s), and $v_{imp}(\rho f_{10}) = 2.9 \times 10^7$ (cm/s).

(Small pilot plant case) (Large power plant case).

significantly lower than needed in most conventional target designs. The corresponding peak compression beam powers needed for each target are estimated to be:

$Ec_{mo_9} \cdot 10^{-9} \cdot \tau_{peak}(r_{c_9}, \rho f_9)^{-1} = 20$ (TW), $Ec_{mo_{10}} \cdot 10^{-9} \cdot \tau_{peak}(r_{c_{10}}, \rho f_{10})^{-1} = 169$ (TW)

(Small pilot plant case) (Large power plant case).

Note that the distributed-radiator target with conventional ignition requires a peak beam power of close to 700 TW [2], so that for a similar type of accelerator used for compression with fast ignition, the cost (for the compression part) should be reduced both because the beam energy and peak power (for compression) is significantly reduced with fast ignition.

The target spot sizes for the compression beams with fast ignition can also be generous as indicated in Fig. 1a, taking into account the much shorter focal lengths required for the small power plant case with a smaller yield and smaller radius chamber, and taking into account the reduced drift pulse compression ratio (by ~3 times) for the large reactor case. Because of the high gain with fast ignition, it would even be acceptable to set the compression beam spot size equal to the entire hohlraum (r_s ~ 3 mm), throwing away the central core of the compression beams with a beam block (a shadow shield not shown in Fig. 1a) that would sit in well in front of the target to shield the ignitor lens and capsule from compression beams coming in nearly parallel with the axis. (the ignitor beam range would go right through such a shine shield). We leave the details of the compression beam acceleration and focusing for future work, as we expect it will be comparable or easier to achieve than in the conventional HIF case. We turn now to the greater challenge of meeting the fast ignitor ion beam requirements.

Fast ignitor ion beam requirements

Ion kinetic energy

Fig. 2 shows the range versus ion linetic energy for a variety of ions. To keep the peak current on the ignitor beam reasonable for transporting and focusing a single ignitor beam, it is desirable to use heavy ions, since at the high velocities required for fast ignition, the heavy ions can still strip off most of their electrons in the target radiators, so that their dE/dx tends to scale as Z^2. This enables one to deliver the required ignition energy with the highest ion kinetic energy and the least current. For a given range, choosing too heavy an ion can lose this advantage when the ion can no longer strip off most of its electrons. The highest electron energy level to which a heavy ion can strip increases with the required ion range, so that the optimal ion mass and Z increases with increasing range requirement. Accordingly, we choose Xenon (Z=54) for the small power plant target ignitor, with

mass $A_9 := 131$ (amu), kinetic energy $T_9 := 2 \cdot 10^{10}$ (eV), and range $R_9 = 1$ (g/cm^2).

and Uranium (Z=92) for the large power plant ignitor, with

mass $A_{10} := 238$ (amu), kinetic energy $T_{10} := 2 \cdot 10^{11}$ (eV), and range $R_{10} = 10$ (g/cm^2).

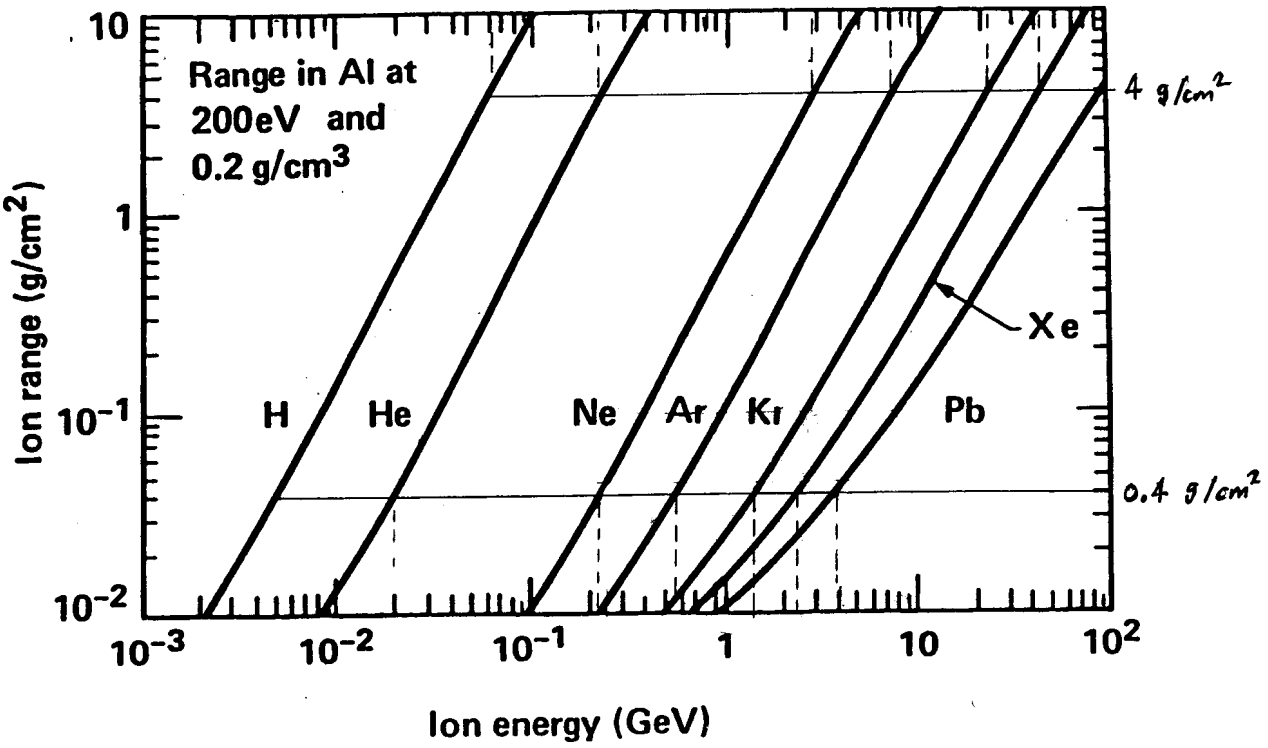

Fig. 2 Ion range (g/cm2) as a function of ion kinetic energy (GeV) for various ions, for low density aluminum radiators. A curve for uranium (not shown) would follow just to the right of the curve for lead (Pb). Note the reduced slope for the heaviest ions at low range, where the ions do not fully strip in the target. For fast ignition, Xenon is the heaviest ion that still fully strips at a range of 1 g/cm^2, while the heaviest ion (uranium) completely strips at 200 GeV in the target for ranges of 10 g/cm^2.

Stripping of these ions at these energies have been extensively studied at the LBNL Bevalac and at the Brookhaven AGS in the 1980's [9]. We need to assign some constants we will be using frequently in subsequent formulas:

$M_p := 1.67 \cdot 10^{-27}$ (kg), the rest mass of a proton,

$e := 1.6 \cdot 10^{-19}$ (C) electron charge,

$c := 3 \cdot 10^{8}$ (m/s) the speed of light,

$m_e := 9.1 \cdot 10^{-31}$ (kg), the electron rest mass

$\varepsilon_o := 8.85 \cdot 10^{-12}$ Vacuum permittivity (Farads/m),

$\mu_o := 4 \cdot \pi \cdot 10^{-7}$ Vacuum permeability (Henrys/m)

$I_o := 3.1 \cdot 10^{7}$ (Amps) -constant in beam perveance)

$$\gamma(T, A) := 1 + \frac{e \cdot T}{A \cdot M_p \cdot c^2}$$ the relativistic gamma factor, with T the kinetic energy in eV, A the atomic mass number Eq. 14

$\beta(T,A) := \sqrt{1-\gamma(T,A)^{-2}}$ the ion velocity normalized to c. Eq. 15

The ignitor ion gammas and betas are

$\gamma(T_9,A_9) = 1.163$ (Small pilot plant case), $\gamma(T_{10},A_{10}) = 1.895$ (Large power plant case).

$\beta(T_9,A_9) = 0.51$ $\beta(T_{10},A_{10}) = 0.849$

The corresponding electron collision energies at the same gammas as the ions are

$(\gamma(T_9,A_9)-1)\cdot m_e\cdot c^2\cdot e^{-1} = 8.3\times 10^4$ (eV), (Small pilot plant case), and

$(\gamma(T_{10},A_{10})-1)\cdot m_e\cdot c^2\cdot e^{-1} = 4.6\times 10^5$ (eV), (Large power plant case).

Both of these electron collision energies are about 3 times the respective ion's K-shell electron binding energies. More than 80% of the 20 GeV Xenon ions will fully strip to (q=54) in 0.045 g/cm^2 aluminum foils with < 2% energy loss, and more than 80% of the Uranium ions will fully strip (q=92) in 0.1 g/cm^2 lead foils with <0.5% energy loss, prior to final focusing to reduce the magnetic fields required to bend the ion trajectories. Nearly all the remaining ions will be in hydrogen or helium-like states. Partial-stripping of such beams can also be done part way through acceleration to reduce the acceleration voltage (as is commonly done in high energy accelerators). For example, Xenon could be stripped to the helium-like state (q=52) in 8 mg/cm^2 aluminum foils (or in equivalent thicknesses of liquid aluminum jets for high pulse rates), at 3 GeV, while Uranium could be stripped to helium-like q=90 in 20 mg/cm^2 lead foils or jets at 30 GeV. Mean-square scattering angles of less than 10^{-4} radians result from these stripping events. Subsequent beam transport through neutralizing plasma, dense plasma lenses, and chamber vapor won't change the ion charge-state significantly enroute to the target, as long as the equivalent areal mass through all such background matter is small compared to 0.1g/cm^2 . For example 100 torr-meters of background gas in the chamber amount to less than 0.01 g/cm^2].

Acceleration gradient- the Dielectric Wall Accelerator

The achievable maximum average acceleration gradient Vg_{max} (V/m) is an important parameter not only in the determination of the accelerator length required to achieve a given voltage, (keeping in mind that fast ignition requires very high acceleration voltages) but also controls the practical limits of longitudinal confinement of the beam against its space-charge field, leading to one of the constraints on the peak beam current. A relatively new accelerator concept [7], called the Dielectric Wall Accelerator (DWA) offers a promising approach to achieving acceleration gradients of 30 MV/m or more, with a very low impedance capable of accelerating 10 kA or more of ion beam currents for short pulses of 1 to 3 ns. Besides fast ignition, this type of accelerator could also provide a relatively compact accelerator for deep cancer therapy with medium-mass ions at ranges of 10 to 15 g/cm^2. Fig. 3 below compares the DWA concept with conventional induction accelerators.

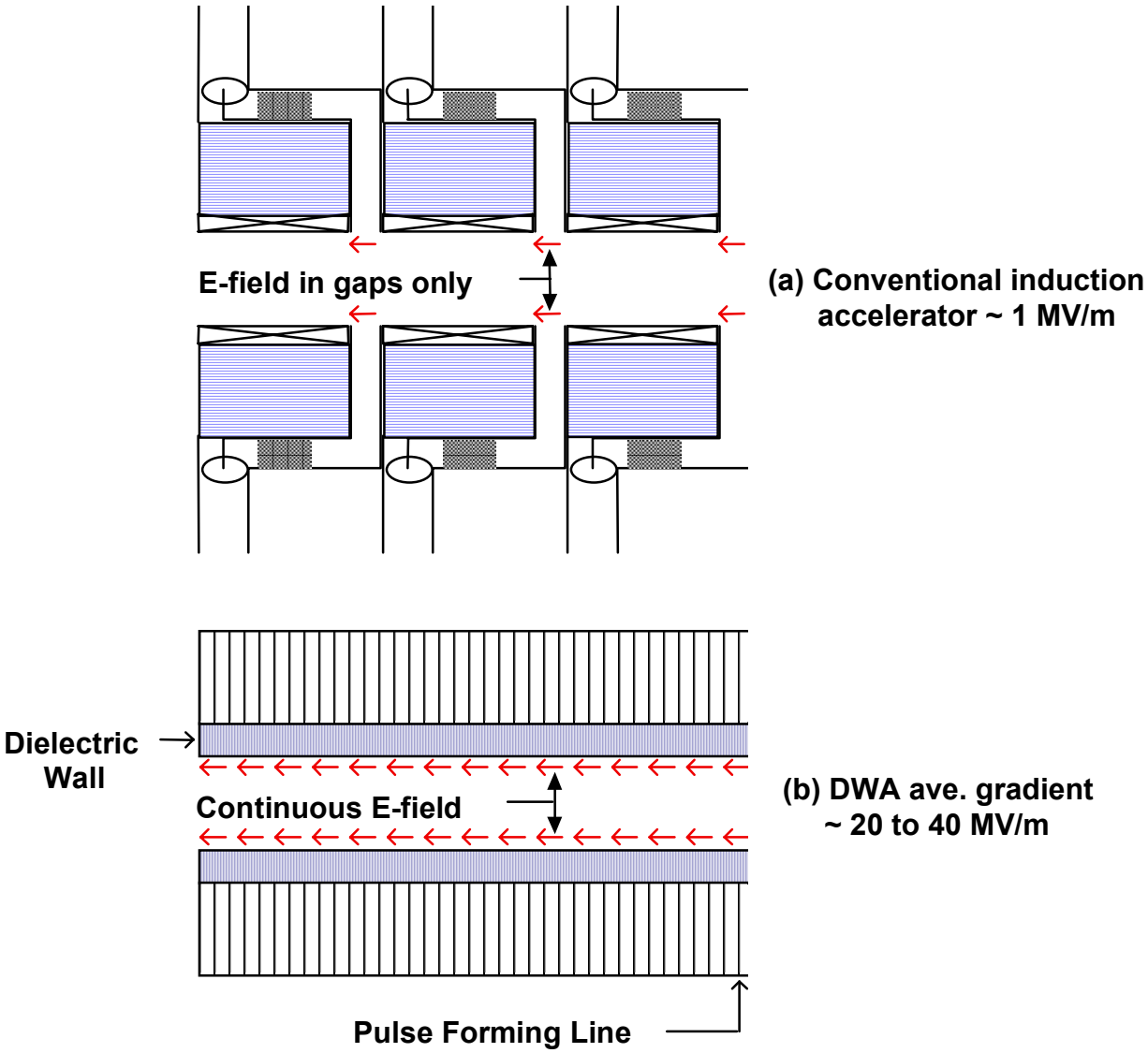

Fig. 3: Schematic cross-sectional views of a conventional induction linac (a) and a dielectric wall accelerator (b). In the induction accelerator the maximum average acceleration gradient is set by breakdown in relatively narrow and widely-spaced gaps, while in the DWA, the average gradient can be much higher with a continuously applied E_z field.

The pulse-forming lines for a DWA can be a series of compact radial Blumleins with alternating slow and fast radial wave propagations speeds, pairs of which are called Asymmetric Blumleins. All of the capacitive energy is compactly stored in the stack of asymmetric Blumleins along the linac. Control of variations in switch timings and charge voltages along the stack can in principle provide traveling waveforms to both accelerate and compress the ion bunches along the linac. Focusing quadrupoles can be placed between modules of such Blumlein stacks for beam confinement. Fig. 4 shows the principle of how such a stack of asymmetric Blumleins can induce accelerating voltage pulses that add in series when the beam passes by.

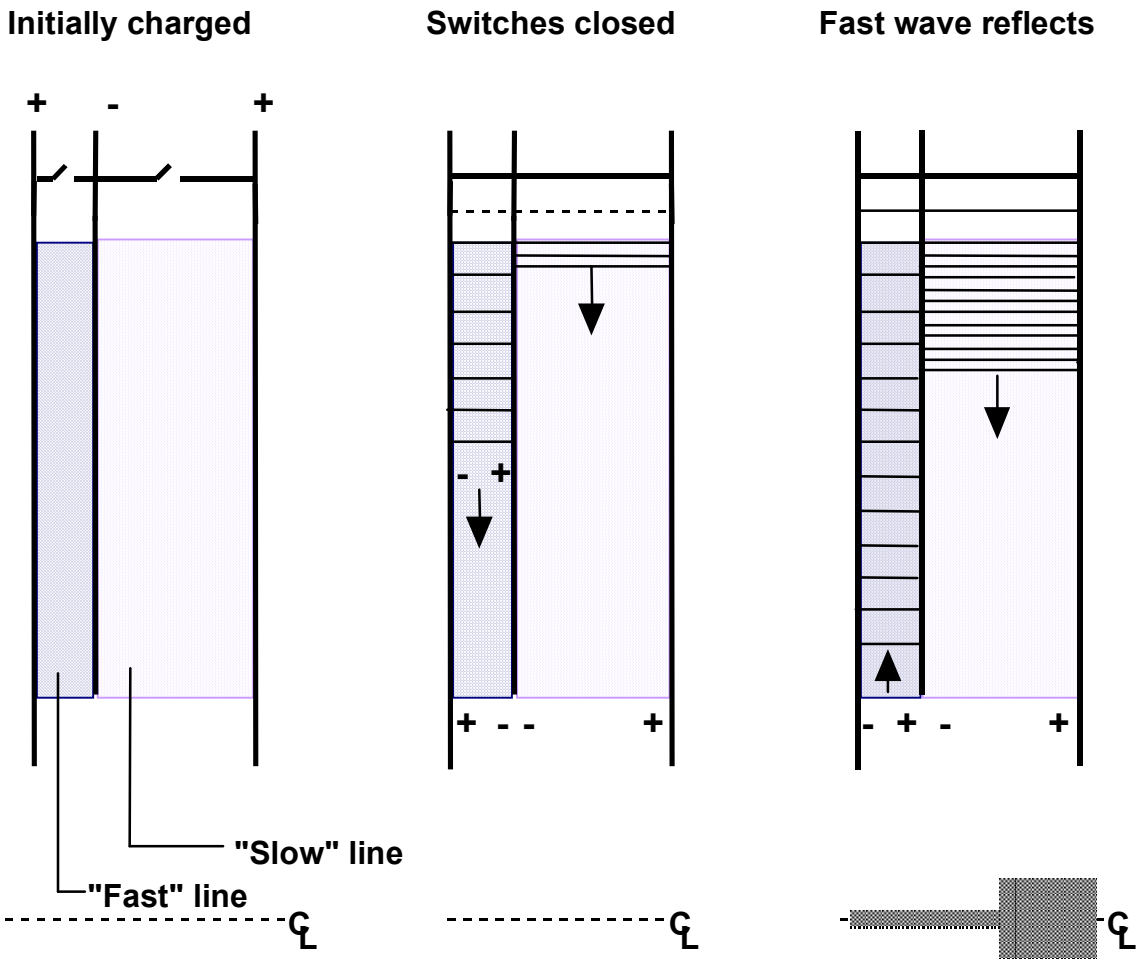

Fig. 4. The Asymmetric Blumlein. The line is pictured at three different times. The initially charged configuration is shown at the left. When the switches close waves carrying polarities opposite to the original charge are propagated radially inward at different speeds (center). When the fast wave reflects from the open circuit at the inner end of the line the polarity of the fast line reverses leading to the appearance of a net voltage across the inner end of the assembly (right).

The pulse length attainable from the Asymmetric Blumlein is equal to the difference in the one way transit times of the slow and fast waves and can be in the range of nanoseconds to tens of nanoseconds, for different dielectric constants between 10 and 80. Asymmetric Blumleins for longer pulses can have a reduced radial size and weight by changing from a sandwich of radial lines to a combination of spiral lines which have a longer path length for a given radius than a simple radial line. [7]. Efficiencies can potentially be in the range of 20 to 40 %.

The breakdown voltage gradient along the dielectric vacuum wall can be increased by use of finely-spaced alternating layers of metal and dielectric, so-called "Microstack" insulators. Fig. 5 shows an example of such an insulator stack tested to >20 MV/m for 20 ns-long pulses. More recent data has exceeded this gradient significantly.

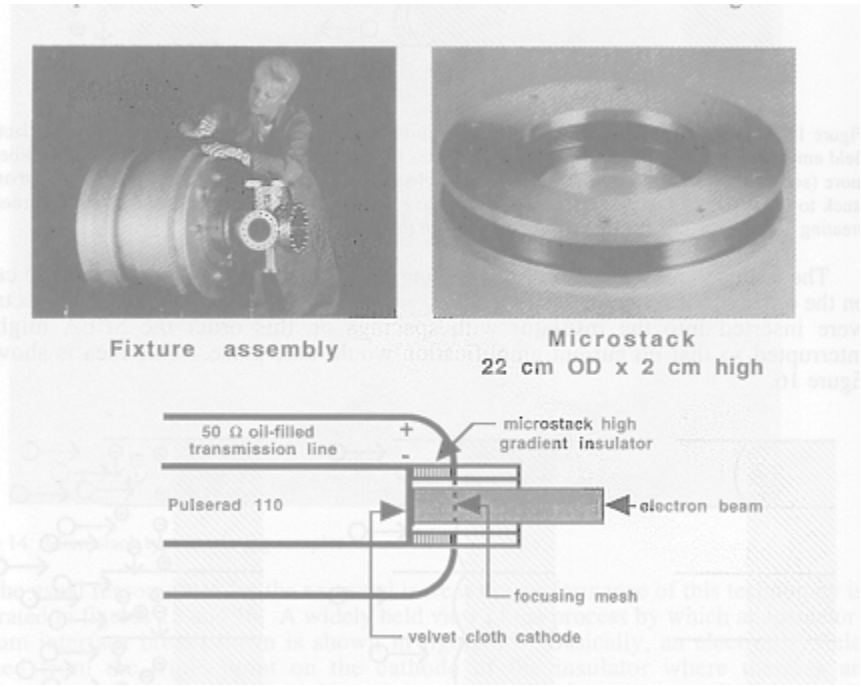

Fig. 5: Microstack insulator for the DWA tested to >20 MV/m at 20 ns pulse lengths.

The maximum breakdown voltage gradient Vg_{max} can be expected to increase with shorter pulses, with a weak empirical scaling with pulse length as $\tau^{1/5}$. Fig. 6 shows the expected scaling of of Vg_{max} with pulse length τ, consistent with the microstack test shown in Fig. 5 at 20 ns. Using the data from the first test (Fig. 5) makes this curve very conservative.

$$Vg_{max}(\tau) := 2\cdot 10^{7}\cdot\left(\frac{20\cdot 10^{-9}}{\tau}\right)^{0.2} \quad \text{(V/m)} \qquad \text{Eq. 16}$$

for $\tau_j := 0.625\cdot 10^{-9}\cdot 2^{(j-1)}$ (s)

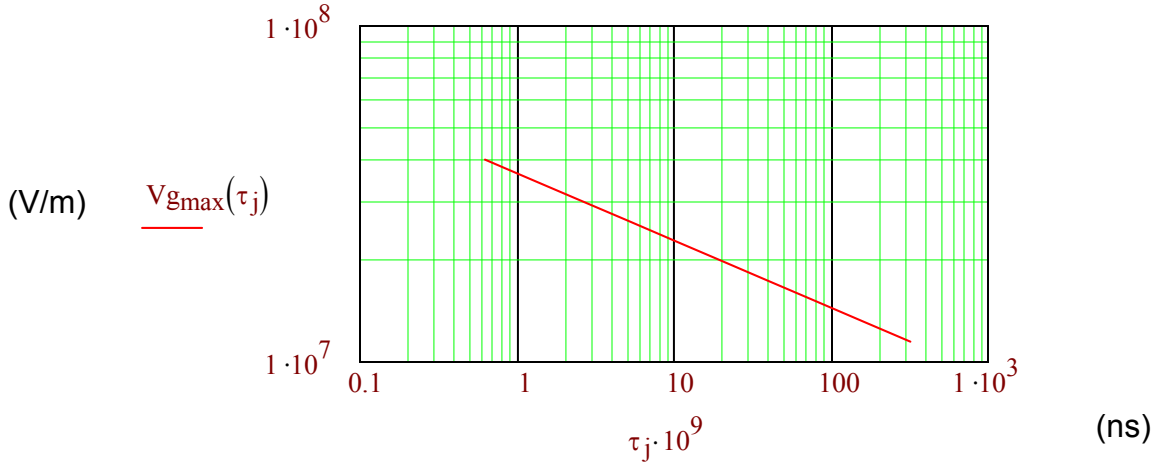

Fig. 6. Expected maximum acceleration voltage gradient (V/m) for the DWA as a function of the beam pulse length τ (ns).

Wall radial electric field: maximum beam line-charge density to avoid breakdown

By Gauss' Law, the radial electric field at the vacuum wall increases with the beam line charge density: Assuming a vacuum wall radius a_w, the radial electric field at the wall is:

$$E_r(I_b, a_w, T, A) := \frac{I_b}{4\cdot\pi\cdot\varepsilon_o\cdot\beta(T,A)\cdot c}\cdot\frac{2}{a_w} \quad \text{(V/m).} \qquad \text{Eq. 17}$$

To avoid breakdown due to E_r, we set a maximum $E_r = Vg_{max}(\tau)$, (assuming radial and axial breakground gradients at the wall are comparable) and then, using Eq. 16 for Vg_{max}, using $\tau_b = L_b / [\beta(T,A)c]$ and using the ignitor beam energy requirement $E_i = I_b \tau_b T / q$ for a given ion charge state q during acceleration, we get a constraint on the maximum beam current equal to

$$I1_{max}(a_w, T, A, q, E_i) := 1.58\cdot 10^8\cdot\left(\frac{T}{q\cdot E_i}\right)^{0.25}\cdot\left(\varepsilon_o\cdot\beta(T,A)\cdot c\cdot a_w\right)^{1.25} \quad \text{(A)} \qquad \text{Eq. 18}$$

It is important to note that to meet the short pulse requirements for fast ignition at the target, that the beam length must be further drift compressed by a factor of twenty or more between the accelerator output and the target with an imposed velocity tilt, and that if the beam were *not* charge-neutralized after acceleration before full drift compression, the radial electric field would increase to 20 x Vg_{max} except that wall electron emission would avalanche first. Accordingly, drift compression must be done with a beam neutralized by some means of introducing or injecting electrons into the beam channel shortly after acceleration. Remaining issues of chromatic aberrations due to the velocity tilt at final focus will be evaluated further on. We next consider a constraint on peak beam current set by longitudinal beam confinement, which, together with Eq. 18, will allow us to determine both the peak current and the ion charge state q consistent with both radial and longitudinal beam space-charge field constraints normalized to Vg_{max}.

Longitudinal beam confinement

For a given product of beam thermal velocity spread $\delta p_z/p_z$ and beam length L_b, Liouville's Theorem limits the maximum beam length compression ratio by velocity tilt between the output of the accelerator and the final focus to the target (the random $\delta p_z/p_z$ increases as the ion bunch length is compressed, and increasing $\delta p_z/p_z$ increases chromatic aberrations of the focal spot, which will be addressed shortly.Thus, achieving shorter pulses at the target for fast ignition also requires shorter pulses in the accelerator. The shortest practical ion pulses in the accelerator are in turn determined by the required energy and range of the ion, and the maximum beam current set by limits on both radial and longitudunal beam space charge fields.

The longitudinal beam space charge field must be counteracted by shaping the accelerating waveform to keep the acceleration gradient higher on the beam tail than on the beam head, to keep the beam bunch from spreading longitudinally. In general, since the minimum ion bunch lengths (~0.5 m) will span many Blumleins in the stack, having to shape the accelerating waveform requires some reduction of the maximum average acceleration gradient, which reductions we would like to keep small. In the DWA case, for example, some

of the periodic asymmetric Blumliens in the stack may either have to be charged to different voltages, or act only on different parts of the beam pulse passing by having shorter pulses, to exert control on the shape of the accelerating waveform.

To keep the beam current below the maximum transportable current in the lower energy end of the accelerator where the ion velocity ($\beta\gamma$) is lower, the ion bunch length L_b has to start out longer from the injector and then be compressed slowly during acceleration down the linac by keeping the local acceleration gradient at the tail of the beam stronger than at the head of the beam. In fact, the low energy front end of a DWA would most likely be an induction linac with metglas cores followed by ferrite cores, to handle the initially longer beam pulses in the front end, where the radial build of a DWA would otherwise become impractically large. We'll leave the front end of the DWA description for future work. In the high energy DWA section, however, further beam length compression by tailoring the local acceleration gradient along the beam pulse in the accelerator becomes impractical when the longitudinal electrostatic field E_z due to the beam space charge becomes a significant fraction f_z of average acceleration gradient acting on the beam. The longitudinal space charge field

$$E_z(I_b, L_b, T, A) := \frac{4 \cdot I_b}{4 \cdot \pi \cdot \varepsilon_o \cdot \beta(T, A) \cdot c \cdot L_b} \quad \text{(V/m)} \qquad \text{Eq. 19}$$

grows both with the current I_b increasing and with the beam length L_b decreasing with the beam going down the accelerator to the point that E_z becomes some significant fraction f_z of the maximum average voltage gradient Vg_{max}. In Eq. 19, the factor of 4 in the numerator accounts for a peak axial electric field at the beam ends due to a parabolic beam line-charge-density profile. Setting $E_z < f_z \times Vg_{max}$, using Eq. 16 for Vg_{max}, using $\tau_b = L_b / [\beta(T,A)c]$ and using the ignitor beam energy requirement $E_i = I_b \tau T / q$ for a given ion charge state q during acceleration, we get another constraint on the peak beam current:

$$I2_{max}(f_z, T, A, q, E_i) := 3 \cdot 10^3 \cdot \left(\frac{q \cdot E_i}{T}\right)^{0.444} \cdot (\varepsilon_o \cdot f_z)^{0.555} \cdot (\beta(T, A) \cdot c)^{1.111} \quad \text{(A)} \qquad \text{Eq. 20}$$

Setting $I1_{max}$ (Eq. 18) = $I2_{max}$ (Eq. 20), we can solve for the ion charge-state:

$$q_a(a_w, f_z, T, A, E_i) := 6.14 \cdot 10^6 \cdot \varepsilon_o \cdot \frac{T}{E_i} \cdot (\beta(T, A) \cdot c)^{0.2} \cdot \frac{a_w^{1.8}}{f_z^{0.8}} \qquad \text{Eq. 21}$$

and, using this q in either Eq. 18 or 20 gives the same peak current:

$$I_{max}(a_w, f_z, T, A, E_i) := I2_{max}(f_z, T, A, q_a(a_w, f_z, T, A, E_i), E_i) \quad \text{(A).} \qquad \text{Eq. 22}$$

With I_b and q determined, we can now calculate the pulse length τ_a and beam length L_b at the output end of the DWA linac required to provide the ignitor energy E_i :

$$\tau_a(a_w, f_z, T, A, E_i) := \frac{q_a(a_w, f_z, T, A, E_i) \cdot E_i}{I_{max}(a_w, f_z, T, A, E_i) \cdot T} \quad \text{(s),} \qquad \text{Eq. 23}$$

$$L_b(a_w, f_z, T, A, E_i) := \beta(T, A) \cdot c \cdot \tau_a(a_w, f_z, T, A, E_i) \quad \text{(m).} \qquad \text{Eq. 24}$$

By inspection, relating both E_r (Eq.17) and E_z (Eq. 19) to Vg_{max}, one notes the beam current and pulse duration actually depend only on β, a_w, and f_z, and the beam length only on a_w and f_z.

Radial beam confinement of ions: maximum transportable beam current.

In the linac, periodic quadrupole magnets are used to radially confine the net force (space-charge minus self-magnetic pinch) on the beam. In some types of accelerators such as the DWA, the accelerating structures can also be designed to also contribute some of the beam focusing, but we will neglect this for simplicity and conservatism. Assuming

superconducting quads with field $B_q := 4$ (T), at a beam radius $a_b := 3 \cdot 10^{-2}$ (m),

the maximum transportable beam current at the high energy end of the accelerator would be

$$I_{tmax}(a_b, B_q, \eta_q, T, A) := 8 \cdot 10^5 \cdot \eta_q \cdot B_q \cdot a_b \cdot \beta(T,A)^2 \cdot \gamma(T,A)^2 \cdot \left(1 - \beta(T,A)^2\right)^{-1} \quad \text{(A)}, \quad \text{Eq. 25}$$

where η_q is the quad occupancy factor (percentage of the linac length occupied by quads). By setting $I_{tmax} = I_{max}$ (Eq. 22), we can solve for the required quad occupancy factor:

$$\eta_q(a_w, a_b, B_q, f_z, T, A, E_i) := 1.25 \cdot 10^{-6} \cdot \frac{I_{max}(a_w, f_z, T, A, E_i) \cdot \left(1 - \beta(T,A)^2\right)}{B_q \cdot a_b \cdot \beta(T,A)^2 \cdot \gamma(T,A)^2} \quad \text{Eq. 26}$$

Finally, we estimate the DWA linac length as twice the "ideal" T / [qVg$_{max}$(1-η_q)] :

$$L_a(a_w, a_b, B_q, f_z, T, A, E_i) := \frac{2 \cdot T \cdot \left(1 - \eta_q(a_w, a_b, B_q, f_z, T, A, E_i)\right)^{-1}}{q_a(a_w, f_z, T, A, E_i) \cdot Vg_{max}\left(\tau_a(a_w, f_z, T, A, E_i)\right)} \quad \text{(m)} \quad \text{Eq. 27}$$

We can now calculate these characteristic DWA parameters for a range of wall radii a_w and ratios $f_z = E_z/V_{gmax}$:

For $i := 1..5$ values of $aw_i := (1 + 0.5 \cdot i) \cdot a_b$, and 10 values $fz_j := 0.1 + 0.02 \cdot j$

we calculate the ranges of beam parmaters for:

Small pilot plant (Case 9)

$$q9_{i,j} := q_a\left(aw_i, fz_j, T_9, A_9, Ei2d_9 \cdot 10^3\right)$$
$$I9_{i,j} := I_{max}\left(aw_i, fz_j, T_9, A_9, Ei2d_9 \cdot 10^3\right)$$
$$\tau 9_{i,j} := \tau_a\left(aw_i, fz_j, T_9, A_9, Ei2d_9 \cdot 10^3\right)$$
$$Lb9_{i,j} := L_b\left(aw_i, fz_j, T_9, A_9, Ei2d_9 \cdot 10^3\right)$$
$$\eta 9_{i,j} := \eta_q\left(aw_i, a_b, B_q, fz_j, T_9, A_9, Ei2d_9 \cdot 10^3\right)$$
$$La9_{i,j} := L_a\left(aw_i, a_b, B_q, fz_j, T_9, A_9, Ei2d_9 \cdot 10^3\right)$$

Large power plant (Case 10):

$$q10_{i,j} := q_a\left(aw_i, fz_j, T_{10}, A_{10}, Eimo_{10} \cdot 10^3\right)$$
$$I10_{i,j} := I_{max}\left(aw_i, fz_j, T_{10}, A_{10}, Eimo_{10} \cdot 10^3\right)$$
$$\tau 10_{i,j} := \tau_a\left(aw_i, fz_j, T_{10}, A_{10}, Eimo_{10} \cdot 10^3\right)$$
$$Lb10_{i,j} := L_b\left(aw_i, fz_j, T_{10}, A_{10}, Eimo_{10} \cdot 10^3\right)$$
$$\eta 10_{i,j} := \eta_q\left(aw_i, a_b, B_q, fz_j, T_{10}, A_{10}, Eimo_{10} \cdot 10^3\right)$$
$$La10_{i,j} := L_a\left(aw_i, a_b, B_q, fz_j, T_{10}, A_{10}, Eimo_{10} \cdot 10^3\right)$$

Ion charge states

Note: ignore $q_9 > q_{max} = 54$ for lowest f_z and largest $a_{w\,->}$

$fz_1 = 0.12 \qquad fz_5 = 0.2 \qquad fz_{10} = 0.3$

$aw_i =$

0.045
0.06
0.075
0.09
0.105

$$q9 = \begin{pmatrix} 14 & 13 & 11 & 10 & 9 & 9 & 8 & 8 & 7 & 7 \\ 24 & 21 & 19 & 17 & 16 & 15 & 14 & 13 & 12 & 11 \\ 36 & 32 & 28 & 26 & 24 & 22 & 20 & 19 & 18 & 17 \\ 50 & 44 & 39 & 36 & 33 & 30 & 28 & 27 & 25 & 24 \\ 65 & 58 & 52 & 47 & 43 & 40 & 38 & 35 & 33 & 31 \end{pmatrix}$$

$$q10 = \begin{pmatrix} 19 & 17 & 15 & 14 & 13 & 12 & 11 & 10 & 10 & 9 \\ 32 & 29 & 26 & 23 & 22 & 20 & 19 & 18 & 16 & 16 \\ 49 & 43 & 39 & 35 & 32 & 30 & 28 & 26 & 25 & 23 \\ 67 & 60 & 54 & 49 & 45 & 42 & 39 & 36 & 34 & 32 \\ 89 & 79 & 71 & 64 & 59 & 55 & 51 & 48 & 45 & 43 \end{pmatrix}$$

$a_b = 0.03$ (m)

$j =$

1
2
3
4
5
6
7
8
9
10

$fz_j =$

0.12
0.14
0.16
0.18
0.2
0.22
0.24
0.26
0.28
0.3

Peak currents (kA)

Currents of a single DWA beam for the ignitor energy.

$$\frac{I9}{10^3} = \begin{pmatrix} 10 & 11 & 11 & 11 & 11 & 12 & 12 & 12 & 12 & 12 \\ 13 & 13 & 14 & 14 & 14 & 14 & 15 & 15 & 15 & 15 \\ 15 & 16 & 16 & 17 & 17 & 17 & 18 & 18 & 18 & 18 \\ 18 & 18 & 19 & 19 & 20 & 20 & 20 & 21 & 21 & 21 \\ 20 & 21 & 21 & 22 & 22 & 23 & 23 & 23 & 24 & 24 \end{pmatrix}$$

$$\frac{I10}{10^3} = \begin{pmatrix} 19 & 19 & 20 & 20 & 21 & 21 & 22 & 22 & 22 & 23 \\ 24 & 24 & 25 & 26 & 26 & 27 & 27 & 28 & 28 & 28 \\ 28 & 29 & 30 & 31 & 31 & 32 & 33 & 33 & 34 & 34 \\ 33 & 34 & 35 & 36 & 36 & 37 & 38 & 38 & 39 & 39 \\ 37 & 38 & 39 & 40 & 41 & 42 & 43 & 43 & 44 & 44 \end{pmatrix}$$

Pulse durations (ns)

$$\frac{\tau 9}{10^{-9}} = \begin{pmatrix} 4.7 & 4.1 & 3.6 & 3.2 & 2.8 & 2.6 & 2.4 & 2.2 & 2 & 1.9 \\ 6.3 & 5.4 & 4.7 & 4.2 & 3.8 & 3.4 & 3.2 & 2.9 & 2.7 & 2.5 \\ 7.9 & 6.8 & 5.9 & 5.3 & 4.7 & 4.3 & 4 & 3.6 & 3.4 & 3.2 \\ 9.5 & 8.1 & 7.1 & 6.3 & 5.7 & 5.2 & 4.7 & 4.4 & 4.1 & 3.8 \\ 11.1 & 9.5 & 8.3 & 7.4 & 6.6 & 6 & 5.5 & 5.1 & 4.7 & 4.4 \end{pmatrix}$$

Note that DWA Blumlein radial builds scale with pulse durations.

$$\frac{\tau 10}{10^{-9}} = \begin{pmatrix} 2.8 & 2.4 & 2.1 & 1.9 & 1.7 & 1.6 & 1.4 & 1.3 & 1.2 & 1.1 \\ 3.8 & 3.3 & 2.8 & 2.5 & 2.3 & 2.1 & 1.9 & 1.8 & 1.6 & 1.5 \\ 4.7 & 4.1 & 3.6 & 3.2 & 2.8 & 2.6 & 2.4 & 2.2 & 2 & 1.9 \\ 5.7 & 4.9 & 4.3 & 3.8 & 3.4 & 3.1 & 2.8 & 2.6 & 2.4 & 2.3 \\ 6.6 & 5.7 & 5 & 4.4 & 4 & 3.6 & 3.3 & 3.1 & 2.8 & 2.7 \end{pmatrix}$$

Beam lengths (m)

(At high energy end of the DWA)

$fz_1 = 0.12$ $fz_5 = 0.2$ $fz_{10} = 0.3$

$aw_i =$

0.045
0.06
0.075
0.09
0.105

$$Lb9 = \begin{pmatrix} 0.73 & 0.62 & 0.54 & 0.48 & 0.44 & 0.4 & 0.36 & 0.33 & 0.31 & 0.29 \\ 0.97 & 0.83 & 0.73 & 0.64 & 0.58 & 0.53 & 0.48 & 0.45 & 0.41 & 0.39 \\ 1.21 & 1.04 & 0.91 & 0.81 & 0.73 & 0.66 & 0.6 & 0.56 & 0.52 & 0.48 \\ 1.45 & 1.24 & 1.09 & 0.97 & 0.87 & 0.79 & 0.73 & 0.67 & 0.62 & 0.58 \\ 1.69 & 1.45 & 1.27 & 1.13 & 1.02 & 0.92 & 0.85 & 0.78 & 0.73 & 0.68 \end{pmatrix}$$

$$Lb10 = \begin{pmatrix} 0.73 & 0.62 & 0.54 & 0.48 & 0.44 & 0.4 & 0.36 & 0.33 & 0.31 & 0.29 \\ 0.97 & 0.83 & 0.73 & 0.64 & 0.58 & 0.53 & 0.48 & 0.45 & 0.41 & 0.39 \\ 1.21 & 1.04 & 0.91 & 0.81 & 0.73 & 0.66 & 0.6 & 0.56 & 0.52 & 0.48 \\ 1.45 & 1.24 & 1.09 & 0.97 & 0.87 & 0.79 & 0.73 & 0.67 & 0.62 & 0.58 \\ 1.69 & 1.45 & 1.27 & 1.13 & 1.02 & 0.92 & 0.85 & 0.78 & 0.73 & 0.68 \end{pmatrix}$$

Quad occupancy factors

$B_q = 4$ (T)

@

$a_b = 0.03$ (m)

$j =$ $fz_j =$

j	fz_j
1	0.12
2	0.14
3	0.16
4	0.18
5	0.2
6	0.22
7	0.24
8	0.26
9	0.28
10	0.3

$$\eta 9 = \begin{pmatrix} 0.22 & 0.23 & 0.24 & 0.24 & 0.25 & 0.25 & 0.26 & 0.26 & 0.27 & 0.27 \\ 0.28 & 0.29 & 0.3 & 0.31 & 0.31 & 0.32 & 0.32 & 0.33 & 0.33 & 0.34 \\ 0.34 & 0.35 & 0.36 & 0.36 & 0.37 & 0.38 & 0.39 & 0.39 & 0.4 & 0.4 \\ 0.39 & 0.4 & 0.41 & 0.42 & 0.43 & 0.44 & 0.45 & 0.45 & 0.46 & 0.47 \\ 0.44 & 0.45 & 0.47 & 0.48 & 0.49 & 0.5 & 0.51 & 0.51 & 0.52 & 0.53 \end{pmatrix}$$

$$\eta 10 = \begin{pmatrix} 0.02 & 0.02 & 0.02 & 0.02 & 0.02 & 0.02 & 0.02 & 0.02 & 0.02 & 0.03 \\ 0.03 & 0.03 & 0.03 & 0.03 & 0.03 & 0.03 & 0.03 & 0.03 & 0.03 & 0.03 \\ 0.03 & 0.03 & 0.03 & 0.03 & 0.04 & 0.04 & 0.04 & 0.04 & 0.04 & 0.04 \\ 0.04 & 0.04 & 0.04 & 0.04 & 0.04 & 0.04 & 0.04 & 0.04 & 0.04 & 0.04 \\ 0.04 & 0.04 & 0.04 & 0.05 & 0.05 & 0.05 & 0.05 & 0.05 & 0.05 & 0.05 \end{pmatrix}$$

Nominal linac lengths (m)

Note: The DWA Blumlein stacks occupy only $0.5\ (1\text{-}\eta_q) \times L_a$

$$La9 = \begin{pmatrix} 136 & 150 & 164 & 178 & 190 & 203 & 215 & 227 & 239 & 250 \\ 93 & 103 & 113 & 122 & 131 & 140 & 149 & 158 & 166 & 174 \\ 70 & 78 & 86 & 94 & 101 & 108 & 115 & 122 & 129 & 135 \\ 57 & 64 & 70 & 77 & 83 & 89 & 95 & 101 & 107 & 113 \\ 49 & 55 & 61 & 66 & 72 & 78 & 83 & 89 & 94 & 100 \end{pmatrix}$$

$$La10 = \begin{pmatrix} 715 & 785 & 850 & 913 & 973 & 1031 & 1087 & 1141 & 1193 & 1244 \\ 454 & 498 & 540 & 580 & 618 & 655 & 690 & 725 & 758 & 790 \\ 319 & 350 & 380 & 408 & 435 & 461 & 486 & 510 & 534 & 557 \\ 240 & 263 & 285 & 307 & 327 & 346 & 365 & 384 & 401 & 418 \\ 188 & 207 & 224 & 241 & 257 & 272 & 287 & 301 & 315 & 329 \end{pmatrix}$$

Selection of accelerator parameters for final focusing analysis

At this point we make a preliminary selection of accelerator parameters from the above sets for the small and large power plant cases, for further analysis of final focusing. The most important parameter affected by the choice of a_w and f_z is the ion charge state q under acceleration. Assuming that complete stripping is not induced until the ion beam gets very close to the target, the chosen charge state q in the accelerator determines the degree to which the beam space-charge fields must be neutralized by injection of electrons after acceleration and before drift compression in a solenoid transport section. Although the model derives self-consistent sets of charge states, the choices should prudently be taken at the atomic shell edges, to facilitate more uniform charge-state production either by laser-field ionization, or by stripping in a foil or liquid metal jet. Staying a factor of two below absorption edge energies means all electron levels below that absorption level will tend to cleanly strip (actual ionic ionization energy levels are ~ 20 to 50 % higher than absorption edge levels).

For Xenon, the ion example for small pilot plant targets, the absorption edge energies and corresponding ion charge states (stripped just below that absorption edge, before the next filled shell is ionized) are: 208 eV (q=8, N-shell), 1.14 keV, (q=26, M-shell), 5.45 keV (q=44, L shell) and 36 keV (q=52, K shell). For Uranium (the ion choice for large power plants), the edges are at 320 eV (q=28, O-shell), 1.4 kev (q=46, N-shell), 5.5 keV (q=64, M-shell), 21 keV (q=82, L-shell), and 115 keV (q=90, K-shell). Looking at the above sets of accelerator cases, we make a preliminary selection of q=26 for Xenon Case 9, and q=90 for Uranium Case 10. For Uranium, we have to invoke stripping (rather than laser-field ionization) at 30 GeV to get the helium-like state at q=90, in order to make the accelerator length reasonable. The choice of q =26 for Xenon is a compromise between accelerator length and quad occupancy factor, as well as the recognition that higher charge states for acceleration would be more difficult to produce by laser field ionization, and that stripping is not so clean in charge-state distribution for any stripping less than helium-like. For these choices, we list the corresponding accelerator parameters from the above set of accelerator parameters:

Table 2 Linac parameters	Small target, Xenon ignitor,		Large target, Uranium ignitor	
Atomic mass	$A_9 = 131$	(amu)	$A_{10} = 238$	(amu)
Ion energy	$T_9 \cdot 10^{-9} = 20$	(GeV)	$T_{10} \cdot 10^{-9} = 200$	(GeV)
Charge state	$q9_{3,4} = 26$		$q10_{5,1} + 1 = 90$	
Linac voltage	$T_9 \cdot 10^{-6} \cdot (q9_{3,4})^{-1} = 775$	(MV)	$T_{10} \cdot 10^{-6} \cdot (q10_{5,1})^{-1} = 2248$	(MV)
Peak current	$I9_{3,4} \cdot 10^{-3} = 16.6$	(kA)	$I10_{5,1} \cdot 10^{-3} = 37$	(kA)
Pulse duration	$\tau 9_{3,4} \cdot 10^{9} = 5.3$	(ns)	$\tau 10_{5,1} \cdot 10^{9} = 6.6$	(ns)
Bunch length	$Lb9_{3,4} = 0.81$	(m)	$Lb10_{5,1} = 1.69$	(m)
Accel gradient	$Vg_{max}(\tau 9_{3,4}) \cdot 10^{-6} = 26.1$	(MV/m)	$Vg_{max}(\tau 10_{5,1}) \cdot 10^{-6} = 24.9$	(MV/m)
Quad occupancy	$\eta 9_{3,4} = 0.36$		$\eta 10_{5,1} = 0.04$	
Linac length	$La9_{3,4} = 94$	(m)	$La10_{5,1} = 188$	(m)
Linac bore radius	$aw_3 \cdot 10^{2} = 7.5$	(cm)	$aw_5 \cdot 10^{2} = 10.5$	(cm)

Neutralization of beam space charge and focusing to target

Fig. 6 shows a scheme for neutralizing, compressing, and focusing fast ignitor beams.

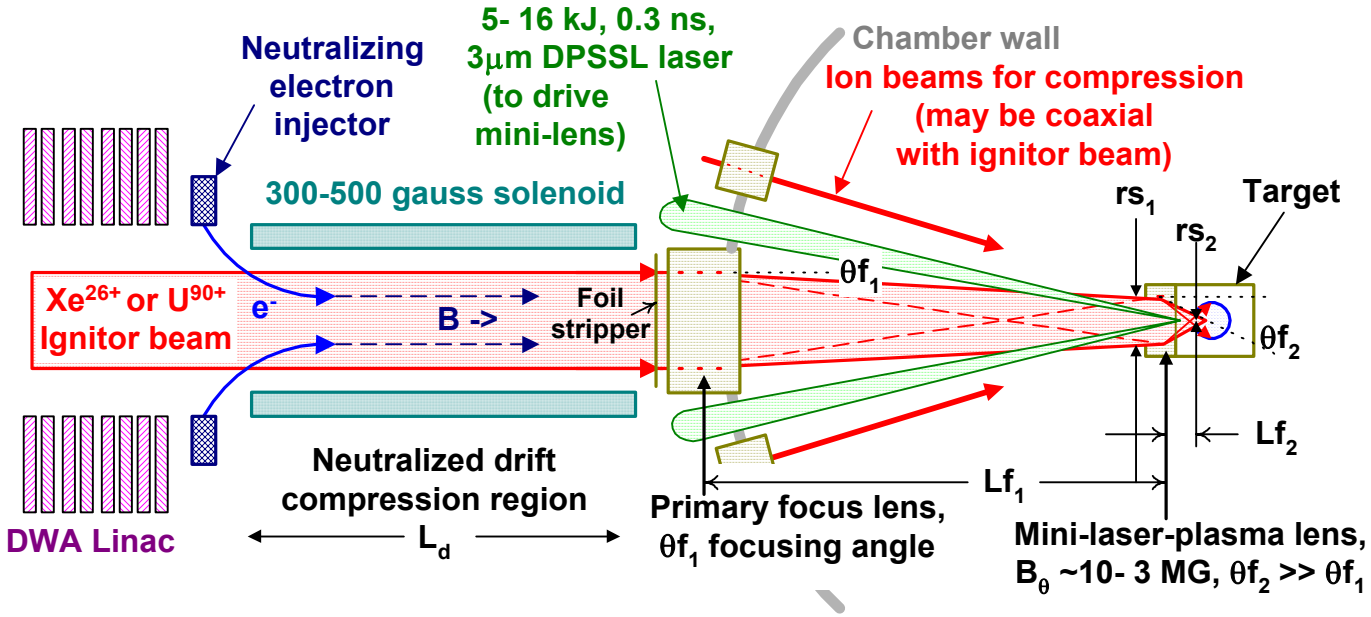

Fig. 6. A conceptual approach to neutralizing, drift-compressing, and focusing fast ignitor ion beams to a single-ended illuminated indirect-drive target [Not drawn-to-scale; all angles exagerated]. The case shown has angular separation of compression and ignitor beams, each beam having its own quadrupole focusing lens near the chamber wall. Alternately, compression and ignitor beams may be sequenced coaxially through an extension and increase of the solenoid field to focus to the target. In either case, the ignitor beam has an additional mm-size laser-driven plasma lens with a stripper foil built into the target (more detail shown in Fig. 1). The ignitor beam is both charge and current-neutralized all the way to the target.

Charge and current-neutralized drift compression

As the beam radial electric field at the end of the accelerator is already at the wall breakdown limit, further pulse compression after acceleration requires charge neutralization by injection of electrons as indicated by the electrun gun at the entrance to the solenoid transport line in Fig. 6. Electrons are injected instead of drawn from a cold plasma because 2-D Particle-In-Cell simulations [10] of neutralization of high-q heavy-ion beams with background plasma shows incomplete neutralization due to (a) cold plasma ions cannot move fast enough, and (b), initially-cold electrons heat up by falling radially into the beam potential well, causing strong radial non-linearities in residual electric fields. A cold electron source within the beam channel neutralizes better by minimizing such radial electron motion [10], but the fast ions still create a potential of order 0.5 m_e v_{beam}^2 in order to pull the cold electrons up to the speed of the beam. In this case, the fast ignitor beam requires 80 kV to 460 kV potentials to pull cold electrons up to the beam speed for the Xenon and Uranium ignitor cases, respectively, and any non-uniformities in that potential could seriously degrade the ignitor beam emittance. On the other hand, co-injecting 20 to 30 kA of electrons up to those energies along field lines entering the solenoid as in Fig. 6 should be straight-forward. The injected radial profiles of electrons can be carefully controlled to avoid non-linearities, current as well as charge neutralization is provided, and the electron injector energies required per 5-6 ns pulse would be only 10 to 100 joules, respectively.

The subsequent transport of the neutralized beam of ions and electrons for drift pulse compression can use a solenoid with a low-field (B_{sol} ~ few-hundred gauss) sufficient to confine the beam transverse ion "emittance" pressure p_x , where p_x ~10^{-2} ($B_{sol}^2/2\mu_o$) . For coaxial beams, the same solenoid field could be extended and increased ~30 x to the target to focus the beam to < 1 mm radius, eliminating need for any primary focusing lenses.

The drift pulse compression ratios required are equal to the bunch lengths (~100 cm) at the linac output over the bunch lengths required (~cm) for the ignitor pulse durations at the target. For the small and large target cases, these overall compression ratios are

$Cdo_9 := \tau 9_{3,4} \cdot (\tau ig_9)^{-1} \cdot 10^{12}$ $Cdo_9 = 176$ and $Cdo_{10} := \tau 10_{5,1} \cdot (\tau ig_{10})^{-1} \cdot 10^{12}$ $Cdo_{10} = 66$

where the required ignitor pulse durations and bunch lengths at the target are

$\tau ig_9 = 30$ (ps), and $\tau ig_{10} = 100$ (ps), respectively, and

$Lig_9 := \tau ig_9 \cdot 10^{-12} \cdot \beta(T_9, A_9) \cdot c$ (m) $Lig_{10} := \tau ig_{10} \cdot 10^{-12} \cdot \beta(T_{10}, A_{10}) \cdot c$ (m)

$Lig_9 \cdot 100 = 0.46$ (cm), and $Lig_{10} \cdot 100 = 2.55$ (cm), respectively.

Because drift compression is neutralized, the imposed velocity tilt for compression $\delta\beta_{o\beta}$ ($\delta\beta_{o\beta}$ means $\delta\beta/\beta$) is preserved through the focusing lenses, and has to be small enough that chromatic aberrations to the spot size are acceptably small. On the other hand, fast ignitor bunch lengths are short enough out of the linac that very small velocity tilts suffice for pulse compression over reasonable drift lengths. For our cases, we find velocity tilts small enough:

$\delta\beta_{o\beta_9} := 0.014$ and $\delta\beta_{o\beta_{10}} := 0.016$, respectively, if chosen such that the corresponding drift lengths are approximately half as longs as the linac lengths:

$Ld_9 := Lb9_{3,4} \cdot (\delta\beta_{o\beta_9})^{-1}$ $Ld_9 = 58$ (m), and $Ld_{10} := Lb10_{5,1} \cdot (\delta\beta_{o\beta_{10}})^{-1}$ $Ld_{10} = 106$ (m).

We also take the corresponding minimum primary focal lengths set by the respective fusion yields Y and blast survivability of the primary focal lens in Fig. 6 to be

$Lf1_9 := 1.5$ (m) at $Y_{mo_9} = 42$ (MJ) yield, and $Lf1_{10} := 7$ (m) at $Y_{mo_{10}} = 1084$ (MJ).

Because the final bunch lengths are so short at the targets, a significant portion C_{dc} of the overall drift pulse compression ratios C_{do} takes place traversing the chamber:

$Cdc_9 := 1 + Lf1_9 \cdot (Lig_9)^{-1} \cdot \delta\beta_{o\beta_9}$ $Cdc_{10} := 1 + Lf1_{10} \cdot (Lig_{10})^{-1} \cdot \delta\beta_{o\beta_{10}}$

$Cdc_9 = 5.6$ (and) $Cdc_{10} = 5.4$, respectively.

Thus, while the ignitor beam peak currents arriving at the target are

$Iig_9 := I9_{3,4} \cdot \tau 9_{3,4} \cdot (\tau ig_9)^{-1} \cdot 10^{12}$ $Iig_{10} := I10_{5,1} \cdot \tau 10_{5,1} \cdot (\tau ig_{10})^{-1} \cdot 10^{12}$

$Iig_9 \cdot 10^{-6} = 2.9$ (MA), and $Iig_{10} \cdot 10^{-6} = 2.461$ (MA), respectively, the corresponding beam currents at the primary focal lenses are smaller

$Iig_9 \cdot (Cdc_9)^{-1} \cdot 10^{-6} = 0.5$ (MA), and $Iig_{10} \cdot (Cdc_{10})^{-1} \cdot 10^{-6} = 0.5$ (MA), respectively.

Again, because of electron injection, these ion currents would be neutralized.

Beam neutralization in the fusion chamber

One measure of the required *degree* of space-charge field neutralization in the fusion chamber shown in Fig. 6, is to calculate the ratio of ψ_{sc} of the residual space-charge field to that without any neutralization, such that the ignitor beam would, by space-charge effects alone, focus to say, half of a desired spot radius rs_1 at some focus length Lf_1. For the small and large power plant examples, we take the following first spot radii, as a compromise between laser-plasma lens and beam emittance requirements (those determined later on):

$rs1_9 := 1.25\cdot10^{-3}$ (m), and $rs1_{10} := 3.5\cdot10^{-3}$ (m), respectively,

If chromatic abberations due to the above velocity tilt were to contribute say, 10% of these primary spot radii, then the beam radii a_f at the primary focal lenses have to be

$af_9 := \frac{rs1_9}{10}\cdot\left(\delta\beta_{o\beta_9}\right)^{-1}$ $af_9 = 0.01$ (m), and $af_{10} := \frac{rs1_{10}}{10}\cdot\left(\delta\beta_{o\beta_{10}}\right)^{-1}$ $af_{10} = 0.022$ (m).

(We can use $\delta\beta$ (velocity) instead of δp (momentum), since $\delta\beta$ is small in this calculation). These beam radii af at the primary focus give first focusing angles of

$\theta f1_9 := \frac{af_9}{Lf1_9}$ $\theta f1_9 = 6\times10^{-3}$ (radians), and $\theta f1_{10} := \frac{af_{10}}{Lf1_{10}}$ $\theta f1_{10} = 3.1\times10^{-3}$ (radians).

The dimensionless beam perveances required to focus to half of the above primary spot sizes at the respective focusing angles and beam radii are

$$K\left(\theta f_1, a_f, rs_1\right) := \theta f_1^{\,2}\cdot\left(2\cdot\ln\left(\frac{a_f}{0.5\cdot rs_1}\right)\right)^{-1} \qquad \text{Eq. 28}$$

$K\left(\theta f1_9, af_9, rs1_9\right) = 6.7\times10^{-6}$ and $K\left(\theta f1_{10}, af_{10}, rs1_{10}\right) = 1.9\times10^{-6}$

With this dimensionless perveance, the residual space-charge after neutralization must be smaller than the space-charge of an un-neutralized beam by a factor

$$\psi_{sc}\left(\theta f_1, a_f, rs_1, T_f, A, I_b, q\right) := \frac{I_o}{I_b}\cdot K\left(\theta f_1, a_f, rs_1\right)\cdot\left(\beta\left(T_f, A\right)\cdot\gamma\left(T_f, A\right)\right)^3\cdot\frac{A}{2\cdot q} \qquad \text{Eq. 29}$$

$\psi_{sc}\left[\theta f1_9, af_9, rs1_9, T_9, A_9, Iig_9\cdot\left(Cdc_9\right)^{-1}, q9_{3,4}\right] = 2.1\times10^{-4}$ for Xenon, small target,

$\psi_{sc}\left[\theta f1_{10}, af_{10}, rs1_{10}, T_{10}, A_{10}, Iig_{10}\cdot\left(Cdc_{10}\right)^{-1}, q10_{5,1}\right] = 7.3\times10^{-4}$ for Uranium, large target.

For comparison, the ratio of residual beam potentials required to "pull" cold electrons in for neutralization, to the un-neutralized beam potential at the linac output are much larger:

$$\frac{\left(\gamma\left(T_9, A_9\right)-1\right)\cdot m_e\cdot c^2\cdot e^{-1}}{\left(\frac{I9_{3,4}}{4\cdot\pi\cdot\varepsilon_o\cdot\beta\left(T_9, A_9\right)\cdot c}\right)} = 0.085 \qquad \frac{\left(\gamma\left(T_{10}, A_{10}\right)-1\right)\cdot m_e\cdot c^2\cdot e^{-1}}{\left(\frac{I10_{5,1}}{4\cdot\pi\cdot\varepsilon_o\cdot\beta\left(T_{10}, A_{10}\right)\cdot c}\right)} = 0.35$$

This is why electrons need to be injected to velocity-match fast ignitor beams.

Secondary focal lens for fast ignition: a laser-driven plasma lens in the target

To achieve the 10 to 30 x smaller spot sizes required for the ion fast ignitor beam compared to conventional HIF, we employ a two lens final-focus system (See Fig. 1a and Fig. 6), whereby a primary magnetic focal lens at the chamber wall focuses the ignitor beam down to the mm-size spots as in conventional HIF regimes [or, alternatively, a focusing solenoid field is extended to the target], but now instead of hitting the target, the ignitor beam enters a smaller secondary lens built into each target. The secondary "mini-lens) has a much higher focusing magnetic field and correspondingly much sharper focusing angle than the first lens ($\theta f_2 >> \theta f_1$). This scheme is analogous to the use of small secondary plasma mirrors built into the target in two-focal-lens laser-driven fast ignition schemes, whereby the local low f-number lens at the target can achieve a much smaller spot size for a given beam quality than a primary large-f-number lens could achieve from a given large distance from the target. In general, if the first spot radius r_{s1} just before the secondary lens is set by a given beam divergence (emittance) and distance from the first primary lens, the secondary spot radius r_{s2} is smaller than the first spot radius according to

$$rs_2(rs_1, \theta f_1, \theta f_2) := rs_1 \cdot \left(\theta f_1 \cdot \theta f_2^{-1}\right) \qquad \text{(approximation in the limit } \theta f_2 >> \theta f_1\text{).} \qquad \text{Eq. 30}$$

Thus, for our two power plant examples, the secondary lens at the target must achieve

$$\theta f2_9 := \theta f1_9 \cdot rs1_9 \cdot (rs2_9)^{-1} \cdot 10^6 \qquad \theta f2_{10} := \theta f1_{10} \cdot rs1_{10} \cdot (rs2_{10})^{-1} \cdot 10^6$$

$\theta f2_9 = 0.298$ (radians), small target $\qquad \theta f2_{10} = 0.219$ (radians), large target

To create such large secondary focusing angles with high energy fast ignitor beams in a small magnetic lens will require very high magnetic fields. It is advantageous to use first-order magnetic lenes such as the plasma lenses (z-discharges) that are used to focus 12 GeV Ar^{18+} beams from the SIS storage ring at GSI, Darmstadt [11]), and it is advantageous to use the highest charge state possible. We assume that the ignitor beams are fully stripped on a foil near the chamber wall, as indicated in Fig. 6. The local B_θ magnetic field magnitude required to bend the fast ignitor beam over a plasma lens distance equal to say, 50% of the secondary focal length $Lf_2 = rs_1 / \theta f_2$, is given by

$$B_\theta(\theta f_2, q, rs_1, T, A) := 6.4 \cdot \beta(T, A) \cdot \gamma(T, A) \cdot A \cdot \theta f_2^{\,2} \cdot (q \cdot rs_1)^{-1} \qquad \text{Eq. 31}$$

$B\theta 2_9 := B_\theta(\theta f2_9, 54, rs1_9, T_9, A_9) \qquad B\theta 2_9 \cdot 10^{-2} = 6.5$ (MG), 20 GeV Xe^{54+}

$B\theta 2_{10} := B_\theta(\theta f2_{10}, 92, rs1_{10}, T_{10}, A_{10}) \qquad B\theta 2_{10} \cdot 10^{-2} = 3.6$ (MG), 200 GeV U^{92+}

These fields may be difficult to achieve with z-discharges as in the GSI plasma lenses, even at mm-scale. However, Rod Mason (LANL) using the ANTHEM code, has shown that fields over 100 MG can be achieved for the short pulses required for fast ignition, using kJ-class CPA lasers [12]. In addition, experiments a decade ago with 100 J ns pulse CO2 lasers at the ILE, Osaka group [13] have shown that adding an electron collector with a laser entrance hole improves the current generation by providing a better retrun path for the laser-heated electrons [see Fig. 7 below]. The geometry in Fig. 1b incorporates this idea. Roughly speaking, a ~5-50 kJ, 3 μm, 200 ps, Zinc-Selenide DPSSL CPA laser [14] with a ~ 0.5 to 1 mm radius spot on the hohlraum wall would be sufficient to drive such lenses.

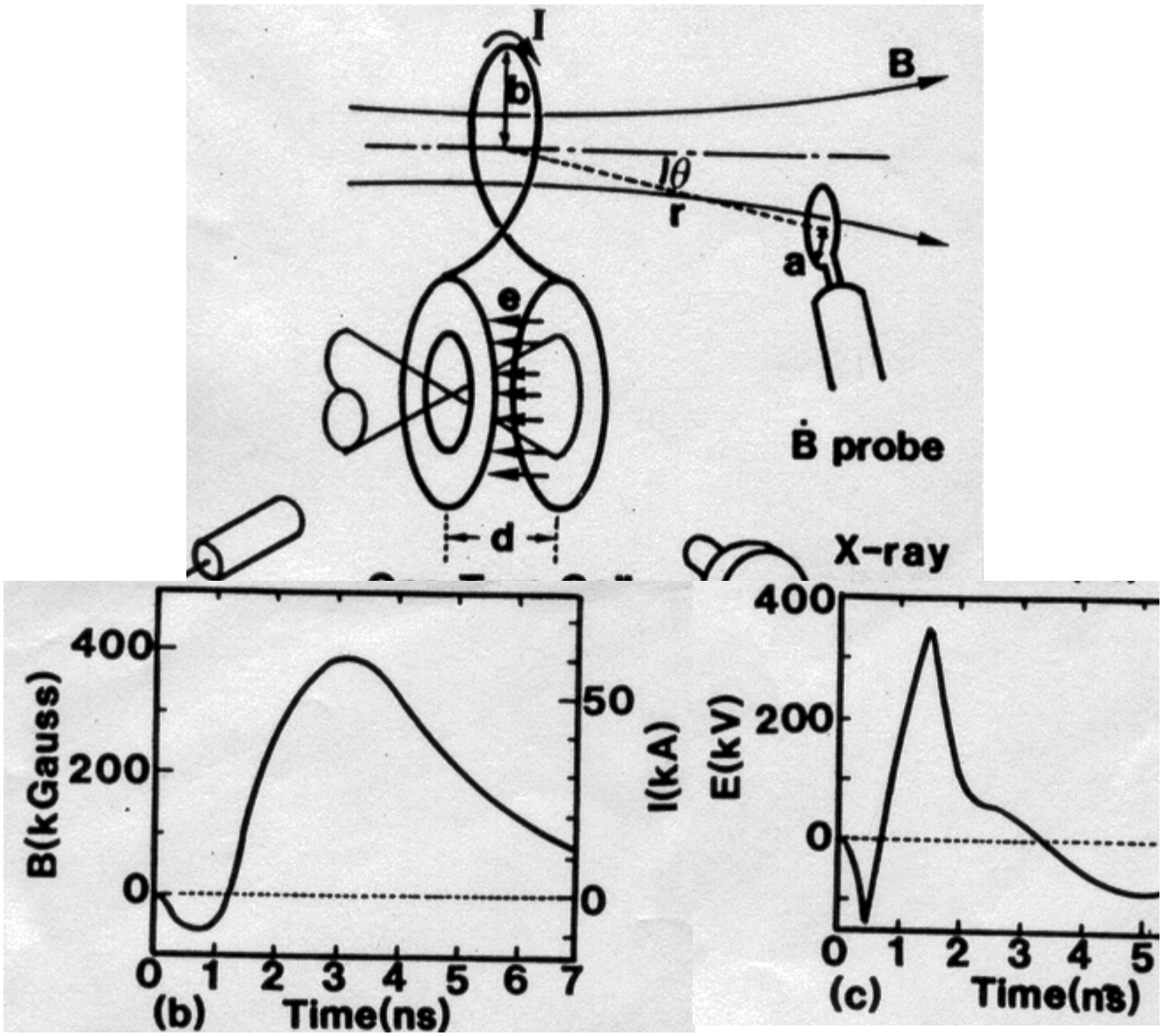

Fig. 7 Experimental demonstration of a laser-driven high field magnet (40 T) in a 2-mm diameter one-turn coil, using a 100 J, CO_2 laser at 1.3 x10^{14} W/cm^2. [From Daido, et. al., ILE Osaka, Reference 13]. The optimum gap d in the generator (Fig. 7a) was found to be 0.5 mm, which produced a maximum of 20 GWe @ 220 kV. The coil magnetic stored energy ~ 10% of the absorbed laser energy. The generator was made of 50 μm-thick copper foil. The pulse length was limited by critical-density plasma crossing the gap. Electron temperatures Te ~ 15 keV were inferred. Note that B_θ fields around the laser focus in the generator can be higher than in the external coil, and this local field is used directly to focus fast ignitor ions as shown in Fig. 1a and Fig. 6

Momentum transfer to the laser-plasma from the beam

The fast-ignitor Xenon and Uranium ion bunches have total relativistic masses of

$Mb_9 := Ei_{2d_9} \cdot 10^3 \cdot (e \cdot T_9)^{-1} \cdot A_9 \cdot M_p \cdot \gamma(T_9, A_9)$ $Mb_{10} := Ei_{mo_{10}} \cdot 10^3 \cdot (e \cdot T_{10})^{-1} \cdot A_{10} \cdot M_p \cdot \gamma(T_{10}, A_{10})$

$Mb_9 = 5.4 \times 10^{-12}$ kg, and $Mb_{10} = 1.3 \times 10^{-11}$ kg, respectively,

while the plasma lens volumes, if filled 30% with 3 μm-critical density of lead plasma ionized to (q/A)ave=0.1, would contain laser plasma masses of

$Mpl_9 := \frac{0.3 \cdot \pi}{\theta f2_9} \cdot (rs1_9)^3 \cdot 10^{26} \cdot 0.1 \cdot 208 \cdot M_p$ $Mpl_{10} := \frac{0.3 \cdot \pi}{\theta f2_{10}} \cdot (rs1_{10})^3 \cdot 10^{26} \cdot 0.1 \cdot 208 \cdot M_p$

$Mpl_9 = 2.1 \times 10^{-8}$ (kg), and $Mpl_{10} = 6.4 \times 10^{-7}$ (kg), respectively.

Assuming radial momentum is conserved with the deflected heavy-ions giving the laser-plasma (with magnetic flux frozen-in on the fast ignitor pulse time-scale) an equal momentum radially outward, the outward radial velocity given to the laser-plasma would be

$vr_9 := \beta(T_9, A_9) \cdot c \cdot \theta f2_9 \cdot Mb_9 \cdot (Mpl_9)^{-1}$ $vr_{10} := \beta(T_{10}, A_{10}) \cdot c \cdot \theta f2_{10} \cdot Mb_{10} \cdot (Mpl_{10})^{-1}$

$vr_9 = 1.1 \times 10^4$ (m/s), and $vr_{10} = 1.1 \times 10^3$ (m/s), respectively,

and the radial displacements in the ignitor pulse times τ_{ig} would be

$vr_9 \cdot \tau ig_9 \cdot 10^{-12} = 3.4 \times 10^{-7}$ m), and $vr_{10} \cdot \tau ig_{10} \cdot 10^{-12} = 1.1 \times 10^{-7}$ (m), respectively,

which are completely negligible compared to the beam and plasma radii.

Two-steam instability and current neutralization in the laser-driven plasma lens

The fast ignitor ion densities in the laser-plasma lens adjacent to the target are:

$nbi_9 := Ei_{2d_9} \cdot 10^3 \cdot \left[e \cdot T_9 \cdot \pi \cdot (rs1_9)^2 \cdot Lig_9 \right]^{-1}$ $nbi_{10} := Ei_{mo_{10}} \cdot 10^3 \cdot \left[e \cdot T_{10} \cdot \pi \cdot (rs1_{10})^2 \cdot Lig_{10} \right]^{-1}$

$nbi_9 = 9.4 \times 10^{20}$ (beam ions/m^3) $nbi_{10} = 1.8 \times 10^{19}$ (beam ions/m^3)

Laser-plasma electron density @ 30% of critical density @ 3 μm = $n_{ple} := 0.3 \cdot 10^{26}$

(plasma electrons/m^3)

Thus, the ratio of ignitor beam ion densities to laser plasma electron densities are

$nbi_9 \cdot n_{ple}^{-1} = 3.1 \times 10^{-5}$ and $nbi_{10} \cdot n_{ple}^{-1} = 5.9 \times 10^{-7}$ respectively.

These smallness of these density ratios, the high laser-plasma electron temperatures T_e > 15 keV associated with intensities $I_{laser}\lambda^2 > 2x10^{16}$ W/cm^2- μm^2), and the steep convergence angles $\theta f_2 > 0.3$ radians, all imply that (a) two-steam instabilities [15] can be avoided, and (b) the insertion of the fast ignitor ion current into the laser-plasma lens can induce sufficient return current to keep the compressed beam well-current-neutralized near the target.

3 μm DPSSL Laser intensity, power, and energy to drive the plasma lens.

Intensities $I_{3\mu m} := 2\cdot 10^{16}\cdot 3^{-2}$ $I_{3\mu m} = 2.2\times 10^{15}$ (W/cm^2)

Energies. We will assume the magnetic field generation efficiency can be 20%, twice that of the ILE experiment, by optimising only the Bθ field around the laser focus (Fig. 1a), eliminating the resistance of an external coil as in Fig. 7:

$E3\mu m_9 := \frac{0.3\cdot\pi}{\theta f2_9}\cdot\left(rs1_9\right)^3\cdot\frac{\left(B\theta 2_9\right)^2}{2\cdot\mu_o}\cdot\frac{1}{0.2}$ (J) $E3\mu m_{10} := \frac{0.3\cdot\pi}{\theta f2_{10}}\cdot\left(rs1_{10}\right)^3\cdot\frac{\left(B\theta 2_{10}\right)^2}{2\cdot\mu_o}\cdot\frac{1}{0.2}$

$E3\mu m_9\cdot 10^{-3} = 5.2$ (kJ), and $E3\mu m_{10}\cdot 10^{-3} = 49$ (kJ).

Multiple DPSSL beams could be used to supply this energy, in a cone array as suggested in Fig. 6.

Powers:

$P3\mu m_9 := I_{3\mu m}\cdot\pi\cdot\left(0.5\cdot rs1_9\cdot 100\right)^2$ (W), and $P3\mu m_{10} := I_{3\mu m}\cdot\pi\cdot\left(0.5\cdot rs1_{10}\cdot 100\right)^2$ (W)

$P3\mu m_9 = 2.7\times 10^{13}$ (W), and $P3\mu m_{10} = 2.1\times 10^{14}$ (W)

Laser pulse lengths

$\tau 3\mu m_9 := E3\mu m_9\cdot\left(P3\mu m_9\right)^{-1}$ (s), and $\tau 3\mu m_{10} := E3\mu m_{10}\cdot\left(P3\mu m_{10}\right)^{-1}$(s).

$\tau 3\mu m_9\cdot 10^9 = 0.192$ (ns) $\tau 3\mu m_{10}\cdot 10^9 = 0.228$ (ns)

Distances from 3μm DPSSL final optic to target mini-lenses, assuming a 0.5 m diameter final optic lens, and 2 x diffraction-limited spot sizes = 0.5 rs_1:

$z_{3\mu m_9} := \frac{2\cdot 0.5}{2\cdot\pi}\cdot rs1_9\cdot\left(3\cdot 10^{-6}\right)^{-1}$ (m), and $z_{3\mu m_{10}} := \frac{2\cdot 0.5}{2\cdot\pi}\cdot rs1_{10}\cdot\left(3\cdot 10^{-6}\right)^{-1}$ (m)

$z_{3\mu m_9} = 66$ (meters). $z_{3\mu m_{10}} = 186$ (meters).

These distances are large because the plasma lens spot requirement is rather large, and this offers a good margin for protecting the final laser optics from the target radiation.

Fast ignitor accelerator beam quality requirements **(ε_n *and* $\delta p/p$)**

The transverse beam temperature ΔT_x determines the normalized beam emittance:

$$\varepsilon_n\left(T,\Delta T_x,A,a_f\right) := 2\cdot\gamma(T,A)\cdot a_f\cdot\sqrt{\frac{e\cdot\Delta T_x}{A\cdot M_p\cdot c^2}}\cdot 10^6 \quad (\pi \text{ mm-mr}), \qquad \text{Eq. 32}$$

where ΔT_x (in eV) is measured at the beam radius a_f just before the primary focus lens (Fig. 6). In Eq. 32, the factor of 10^6 is inserted so that the normalized emittance can be expressed in the usual units of millimeters times milliradians.

The parallel temperature ΔT_z out of the accelerator (a measure of the random thermal spread, not the choherent velocity tilt imposed by the accelerator), together with the beam drift compression ratio C_{df} between the accelerator output and the primary focal lens, determines the normalized momentum spread at the final focus lens:

$$\delta p_{op}\left(T,\Delta T_z,A,C_{df}\right) := \left(\frac{e\cdot\Delta T_z}{A\cdot M_p\cdot c^2}\right)\cdot\frac{C_{df}}{\beta(T,A)^2\cdot\gamma(T,A)} \qquad \text{Eq. 33}$$

where we have made the approximation $\Delta T_z << T$. (δp_{op} = delta p_z / p_z at final focus).

In terms of these transverse and parallel measures of beam quality at the primary focus at distance Lf_1 from the first focus point (see Fig. 6), the beam spot size at the primary focus (again, neglecting space charge effects due to neutralization of the ignitor beam), is given by

$$r_s\left(T,\Delta T_x,\Delta T_z,A,a_f,Lf_1,\theta f_1,C_{df},\delta\beta_{o\beta}\right) := \sqrt{\left(\frac{\varepsilon_n\left(T,\Delta T_x,A,a_f\right)\cdot 10^{-6}}{\beta(T,A)\cdot\gamma(T,A)\cdot\theta f_1}\right)^2 \ \ldots + \left[Lf_1\cdot\theta f_1\cdot\left(6\cdot\delta p_{op}\left(T,\Delta T_z,A,C_{df}\right)\ \ldots + \delta\beta_{o\beta}\right)\right]^2} \quad \text{(m)}, \qquad \text{Eq. 34}$$

In Eq. 34 we have added the coherent velocity tilt $\delta\beta_{o\beta}$ necessary for the ignitor pulse drift to the random (thermal) parallel momentum spread δp_{op}.

Longitudinal momentum spread requirement

Liouville's conservation of phase space preserves the product of fast ignitor bunch length and random thermal momentum spread, so that while the velocity tilt $\delta\beta_{o\beta}$ is constant during the ion bunch drfit compression (assuming the beam space charge is neutralized), the thermal momentum spread increases inversely with the bunch length compression. The maximum thermal momentum spread is set when δp_{op} grows to become comprarable to the coherent velocity tilt $\delta\beta_{o\beta}$, since further bunch compression then stops. Assuming δp_{op} equals $\delta\beta_{o\beta}$ at the target (or laser-plasma lens), we can determine the maximum allowed value of δp_{op} at the primary focus lens and at the accelerator output :

At the primary focus lens: $\delta p_{opf_9} := \delta\beta_{o\beta_9}\cdot(Cdc_9)^{-1}$ $\delta p_{opf_{10}} := \delta\beta_{o\beta_{10}}\cdot(Cdc_{10})^{-1}$

$\delta p_{opf_9} = 2.5\times 10^{-3}$ $\delta p_{opf_{10}} = 3\times 10^{-3}$

At the accelerator output: $\delta p_{opf_9} := \delta\beta_{o\beta_9}\cdot(Cdo_9)^{-1}$ $\delta p_{opf_{10}} := \delta\beta_{o\beta_{10}}\cdot(Cdo_{10})^{-1}$

$\delta p_{opf_9} = 8\times 10^{-5}$ $\delta p_{opf_{10}} = 2.4\times 10^{-4}$

These values of δp_{op} at the primary focus lens are comparable to values typically assumed for conventional HIF, while the values at the accelerator output are about 10x lower due to the use of larger pulse compression ratios (100 x vs 10x) for fast ignition compared to conventional HIF. Thus, for example, better control of pulser jitter (e.g., more expensive pulser regulation to within 0.1 % instead of 1%), may be required to achieve these lower values of longitudinal momentum spread.

Transverse emittance

Using the above values of longitudinal momentum spread at the primary focus lens, and using Eq. 34, we can determine the allowed normalized transverse emittance to meet the primary focal spot size rs_1:

$$\varepsilon_{nf}(T,A,rs_1,Lf_1,\theta f_1,\delta p_{op},\delta\beta_{o\beta}) := 10^6\cdot\beta(T,A)\cdot\gamma(T,A)\cdot\theta f_1\cdot\sqrt{rs_1^{\,2}-\left[Lf_1\cdot\theta f_1\cdot\begin{pmatrix}6\cdot\delta p_{op}\ \ldots\\ +\delta\beta_{o\beta}\end{pmatrix}\right]^2}$$

$\varepsilon nf_9 := \varepsilon_{nf}(T_9,A_9,rs1_9,Lf1_9,\theta f1_9,\delta p_{opf_9},\delta\beta_{o\beta_9})$ (πmm-mr)

$\varepsilon nf_9 = 4.4$ (π mm-mr), for our small pilot plant case, and Eq. 35

$\varepsilon nf_{10} := \varepsilon_{nf}(T_{10},A_{10},rs1_{10},Lf1_{10},\theta f1_{10},\delta p_{opf_{10}},\delta\beta_{o\beta_{10}})$

$\varepsilon nf_{10} = 17.5$ (π mm-mr), for our large power plant case.

The beam emittance requirements for the small pilot plant case are factors of two below those typically assumed for conventional HIF, while the large ignitor case requirement is similar. This is because of the assistance the laser-driven plasma lens provides for focusing. Without such a lens, the beam emittance requirements for fast ignition would be about 10 times more stringent.

IV. Benefits of fast ignition for heavy-ion fusion power plants

Reduction of driver energy and cost

We have used a source-to-target systems code [16] to estimate the minimum-cost of multi-beam induction linac drivers for heavy-ion fusion as a function of the driver beam energy delivered to the target, for a variety of ion species, with results summarized in Fig. 8 below. For conventional HIF targets [2], the driver energy would be delivered in two beam pulses, one prepulse of about 25 ns duration, and one main pulse of about 8 ns duration, that are both converted to x-rays for pulse-shaping in the distributed radiators surrounding the capsule in indirect-drive targets. Such targets would look similar to Fig. 1a except for having two-sided illumination, a larger hohlraum case-to-capsule radius ratio, and no ignitor beam. The systems model assumes one induction linac is used to accelerate a single bundle of beams up to a kinetic energy equal to about 80% of the final energy, at which point about 30 % of the beams are diverted for a target pre-pulse for pulse-shaping). The rest of the beams are further accelerated up to the final kinetic energy for a range R = 0.04 g/cm^2, suitable for the low-density distributed radiators. The model assumes all-superconducting magnetic quadrupoles for beam transport in tightly-packed arrays (no-beam merging), and minimizes the beam radius as the ions accelerate down the linac. The injector pulse duration is also optimized to minimize the entire linac cost.

The direct cost in 97 dollars includes the ion sources and injectors, the induction linac (magnetic cores, quadrupoles, insulators, pulsers and energy strorage), beam transport and drift compression to the target, and the shielded superconducting quadrupole final focus arrays. The number of beams is optimized to minimize the total cost of each integrated system. The unit cost assumptions assume reasonable projected component cost reductions through further R&D to a power plant level of maturity. The total driver capital cost, including indirect costs for a power plant, would be twice the direct costs. For a given range and ion species, the accelerator voltage and volt-seconds (aggregate magnetic core cross-section) optimize to be close to constant with beam energy, so that the total beam current through the accelerator varies linearly with the delivered beam energy. As a result of the magnetic core volume at constant cross-section scaling to a finite minimum as the beam energy and current scale to zero, the best-fit curves to the driver cost versus beam energy closely approximate offset linear curves, which for the following ion species we have studied, all at constant range = 0.04 g/cm^2 for distributed radiator targets, are given approximately by

4 GeV Pb^{1+}	$C_{dPb}(E_d) := 116.84 \cdot E_d + 576.4$	(direct costs in millions of 97 dollars)	Eq. 36
2.5 GeV Xe^{1+}	$C_{dXe}(E_d) := 111.83 \cdot E_d + 398.7$		
1.4 GeV Kr^{1+}	$C_{dKr}(E_d) := 103.59 \cdot E_d + 283.8$		
2.5 GeV Xe^{8+}	$C_{dXe8}(E_d) := 115.02 \cdot E_d + 166.7$		
0.22 GeV Ne^{1+}	$C_{dNe}(E_d) := 116.53 \cdot E_d + 140.5$		

These fits tends to overestimate the costs of the systems code below Ed < 1 MJ by 25 %, but we'll accept this conservatism because we don't assume any "economy of quantity/size" in unit costs used in the systems code which would otherwise penalize such small accelerators.

For $Ed_j := 0.29 \cdot 1.4^{j-1}$ driver energy points, we plot the cost relations of Eq. 36 in Fig 8:

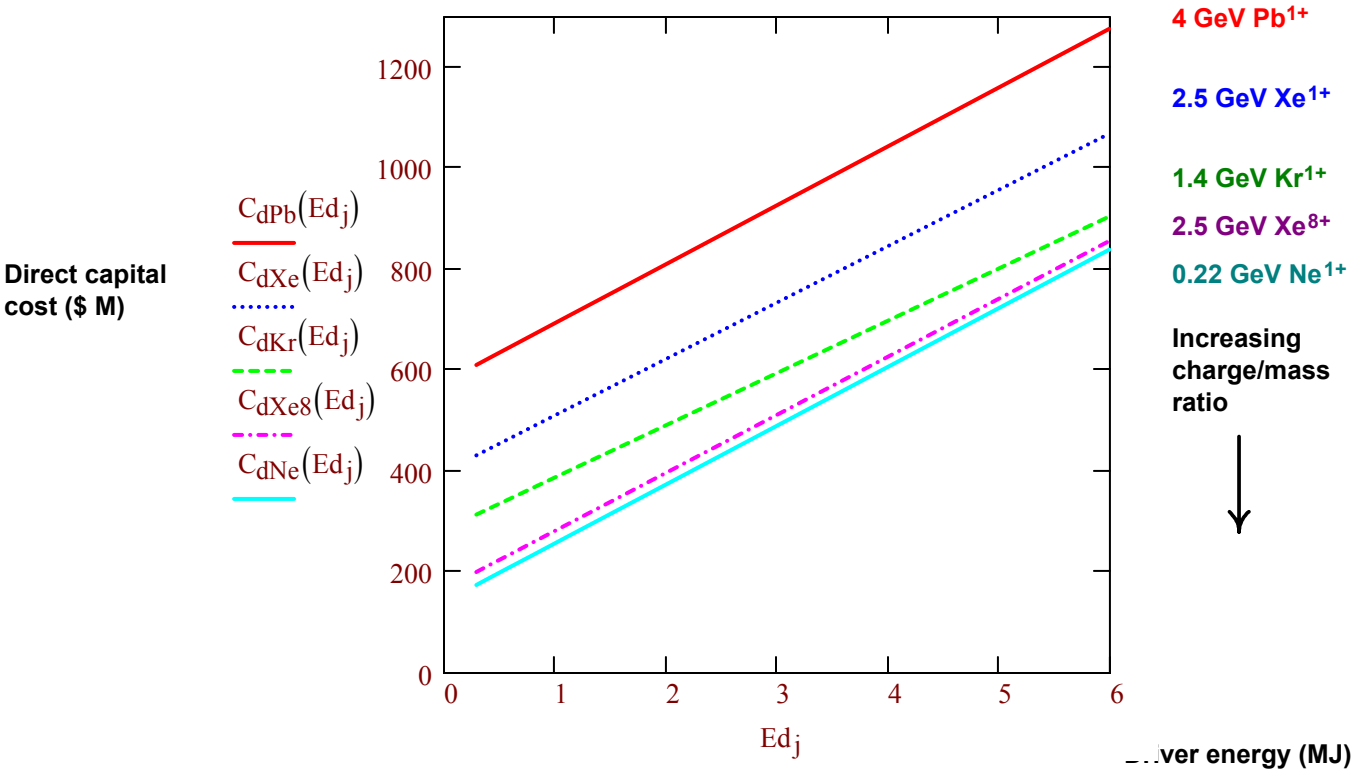

Fig. 8 : Direct capital cost ($M) of induction linac drivers for distributed radiator, indirect-drive targets, as a function of total beam energy E_d (in MJ), for various ion species with range R = 0.04 g/cm^2.

Fig. 8 shows the benefits of using ions with increasing charge-to-mass ratio, which decreases the accelerator voltage and increases the total beam current. Note there is a diminishing reduction in driver cost for charge to mass ratios higher than Xe^{8+} or Ne^{1+}, and focusing also gets more difficult at higher charge-to mass ratio ions, so we will limit our power plant examples to Ne^{+1} for estimating compression beam costs. As for focusing, we note that the small yield case can have a much shorter focal length to the target, while the large target has a much larger hohlraum radius compared to conventional HIF cases, so that realistic solutions for focusing can be expected in future work.

For a nominal induction linac output pulse duration $\tau a := 200$ (ns),

and a peak pulse carying 75 % of the total driver energy, the total beam current I_{tot} through the induction cores at the high energy end of the linac is

$$I_{tot}(Ed, q, \tau a, T) := 0.75 \cdot Ed \cdot 10^3 \cdot q \cdot \tau a^{-1} \cdot T^{-1} \quad \text{(kA)}, \qquad \text{Eq. 37}$$

where E_d is in MJ, τ_a in ns and final ion kinetic energy T in GeV. A rough fit to the systems code accelerator efficiencies (beam energy out over electrical energy in) is given by

$$\eta_d(Ed, q, \tau a, T) := 0.7 \cdot \left(\frac{I_{tot}(Ed, q, \tau a, T)}{17 + I_{tot}(Ed, q, \tau a, T)} \right)^{0.6} \qquad \text{Eq.38}$$

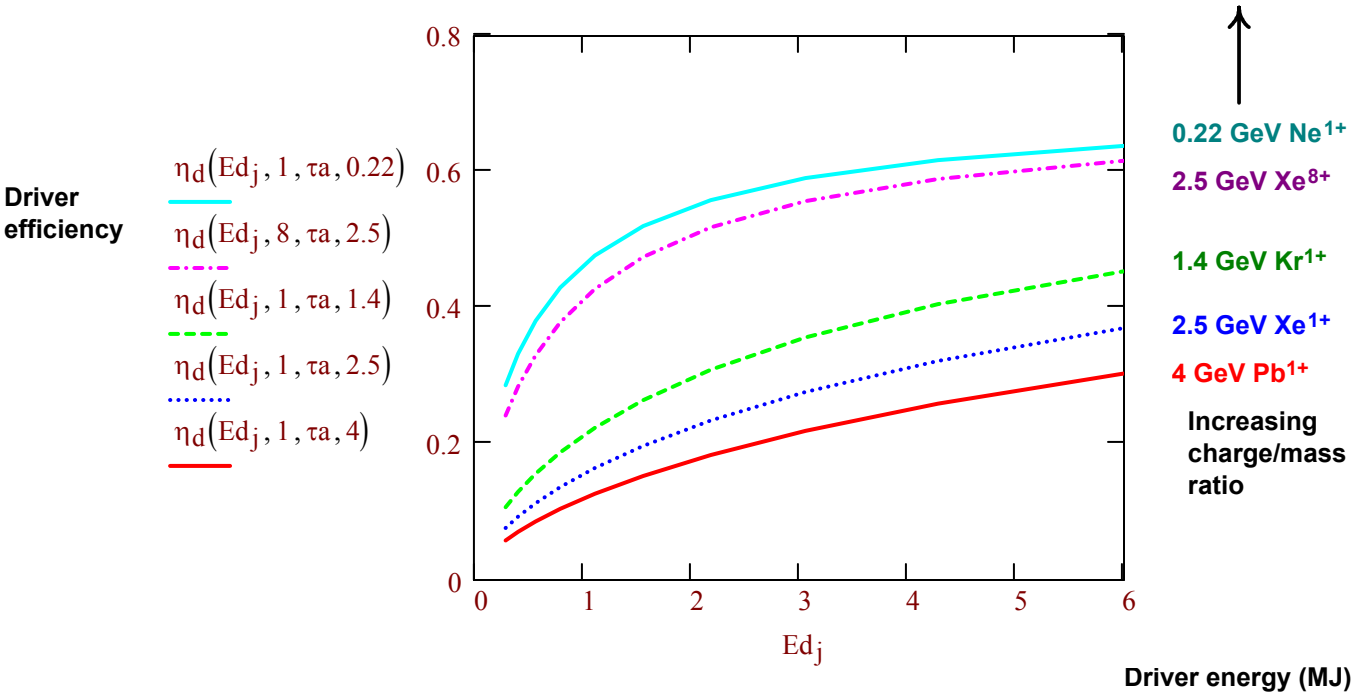

Fig. 9 Induction linac driver efficiency as a function of driver energy Ed (MJ). This efficiency improves with increasing total beam current (either through increasing beam energy E_d or by decreasing accelerator voltage with higher charge-to mass ratio ions, by Eqs. 37 and 38. All efficiencies tend to zero as the driver beam energy and current go to zero, reflecting finite accelerator power consumption due to finite core volume and losses in the limit of zero beam current running through the induction cores.

To model fast ignition cases, we assume the compression beam system uses a similar type of induction linac as in conventional HIF to accelerate similar kinetic energy ions of low range (R~0.04 g/cm^2) at similar-cost-optimized pulse durations in the linac, but delivering somewhat longer compression pulses to the target by reducing the drift compression ratios relative to the conventional HIF case. Lacking a specific design to estimate costs of fast ignitor beams (that would require a separate linac designed specifically for short pulses and high gradients such as the DWA example), we also assume the ignitor beam costs the same per joule as does the compression beams. This crude assumption may have some justification, in that cost-savings for much shorter ignitor linacs at high gradients may be offset by more demanding switching requirements for short pulses. The total driver cost for fast ignition cases could then be estimated from the compression beam model with a higher driver energy in Fig. 8 which would be the sum of compression and ignitor beam energy $E_d = E_c + E_i$. Since the compression energy is large compared to the ignition energy in most fast ignition cases, the total driver cost based on these assumptions would not be so sensitive to the uncertainty in the cost of the ignitor beam. We also assume, lacking more information, that the ignitor beam would have the same efficiency as the compression beams at each total driver energy level. Thus, for our small and large power plant cases with Ne^{1+}, we estimate

$Cd_9 := C_{dNe}\left[\left(Ec_{mo_9} + Ei_{2d_9}\right)\cdot 10^{-3}\right]$ $\quad Cd_9 = 163$ driver cost ($M), and

$\eta d_9 := \eta_d\left[\left(Ec_{mo_9} + Ei_{2d_9}\right)\cdot 10^{-3}, 1, \tau a, 0.22\right]$ $\quad \eta d_9 = 0.23$ efficiency, for the small pilot plant case.

$Cd_{10} := C_{dNe}\left[\left(Ec_{mo_{10}} + Ei_{mo_{10}}\right)\cdot 10^{-3}\right]$ $Cd_{10} = 619$ ($M),

$\eta d_{10} := \eta_d\left[\left(Ec_{mo_{10}} + Ei_{mo_{10}}\right)\cdot 10^{-3}, 1, \tau a, 0.22\right]$ $\eta d_{10} = 0.61$ for the large power plant case.

Liquid-protected chambers: reducing the size and clearing time for small plants

We showed in Section II that with fast ignition, it is possible to achieve very small fusion yields

$Y_{2d_9} = 43$ (MJ)

while still achieving a very high target gain $G_{mo_9} = 253$

and power balance with an $\eta_d G$ product $\eta d_9 \cdot G_{mo_9} = 59$

For an attractive development step to a commerical power plant, fast ignition allows a minimum capital-cost pilot plant in which the reduced fusion yield allows a reduced-radius liquid-protected chamber like HYLIFE-II [17], which not only would cost less, but would allow proportionately shorter chamber clearing times, and proportionately higher pulse repetition rates. Fig. 10 shows a reduced-size HYLIFE-II chamber. In the following power plant descriptions for a small pilot plant based on HYLIFE-II, we use appropriate model descriptions and scalings from both reference [17], and for a multi-unit version [18]. Scaling the HYLIFE-II chamber of 3.5 m radius, which was designed for 350 MJ yield at 6 Hz, by a scaling factor which is the average of the square and cube roots of the yield ratios

$$Fc_9 := \frac{1}{2}\cdot\left(\sqrt{\frac{350}{Y_{2d_9}}} + \sqrt[3]{\frac{350}{Y_{2d_9}}}\right) \qquad Fc_9 = 2.43$$

we can estimate a reduced-scale HYLIFE-II chamber radius for our small yield pilot plant:

$$Rcbr_9 := \frac{3.5}{Fc_9} \quad \text{(m)} \qquad Rcbr_9 = 1.4 \quad \text{(m)}.$$

This reduced chamber radius at small fusion yields supports our choice of a primary focal length of 1.5 m for the small pilot-plant case. For a given molten-salt jet velocity, the HYLIFE-II chamber clears in a time proportional to the linear dimensions of the chamber, so that the maximum chamber pulse repetition rate RR_c set by clearing would also be correspondingly higher than at 3.5 m:

$RRc_9 := 6\cdot Fc_9$ (Hz) $RRc_9 = 14.6$ (Hz)

With a Flibe molten salt blanket energy multiplier $M := 1.18$, this chamber pulse rate would produce an average fusion thermal power per chamber of

$Pth_9 := Y_{2d_9}\cdot M\cdot RRc_9$ $Pth_9 = 740$ (MWth).

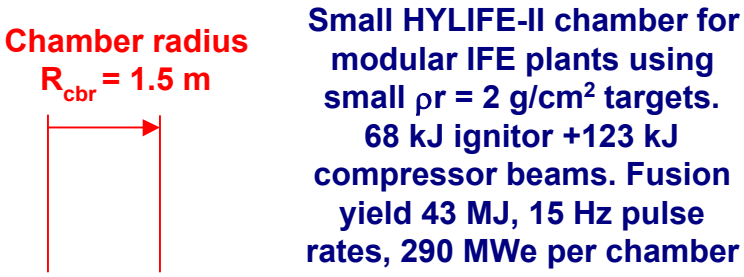

Fig. 10 : A smaller-scale HYLIFE-II chamber (2.4 x smaller in all linear dimensions, compared to a 3.5 m radius, 6 Hz, 350 MJ-yield HYLIFE-II chamber) for reduced fusion yields of 44 MJ from small ρr = 2 g/cm2 ion-fast-ignition targets. Smaller dimensions allow faster clearing and 2. 4 x higher pulse-rates for the same jet velocity. One chamber would serve as a small IFE pilot plant (case 9), producing about 290 MWe with a standard steam cycle, about the same size and power as a typical gas-turbine unit today. The total pilot plant capital cost (direct + indirect) would be $1.5 B. Several such chambers could be driven with a shared driver through a beam switchyard, leading to modular plants that can start small and build in stages to larger plant outputs, since induction accelerators can be designed > 100 Hz pulse rates.

The driver recirculating electric power per chamber at this pulse rate would be

$$Pde_9 := \left(Ec_{mo_9} + Ei_{2d_9}\right)\cdot 10^{-3}\cdot\left(\eta d_9\right)^{-1}\cdot RRc_9 \qquad Pde_9 = 12 \quad \text{(MWe)}.$$

With an auxiliary electric power fraction for pumps equal to $f_{aux} := 0.05$

and a supercritical steam plant net thermal conversion efficiency $\eta_{spp} := 0.43$

the above thermal power would net an electrical ouptut per chamber of

$$Pnet_9 := Pth_9\cdot\eta_{spp}\cdot\left(1 - f_{aux}\right) - Pde_9 \qquad Pnet_9 = 291 \quad \text{(MWe)}.$$

This net electric power ouput level per chamber and chamber size are both comparable to modular gas turbine electric plants with a steam bottoming cycle. The next analysis compares the annual cost of capital for this type of modular fusion plant with one driver and target factory driving multiple fusion chamber units with the annual cost of natural gas for a modular gas turbine plant of similar total electric output, as a function of the number of modular units. We will use the multi-unit HYLIFE-II model [18] for the estimating the costs, escalating the 1993 costs to 1997 costs by a factor of 1.125

Electric plants using small fast ignition targets and modular HYLIFE-II chambers.

In the following, following ref. [18], we assume a variable number Nu of modular chambers and steam plants, with reduced costs due to the multiplicity of units by a factor cd(Nu):

$$Nu_i := 2^{i-1} \qquad cd(Nu) := \left[0.2 + 0.8\cdot Nu\cdot 0.97^{\left(\frac{\ln(Nu)}{\ln(2)}\right)}\right]$$

Nu_i	$cd(Nu_i)$	$cd(Nu_i)\cdot(Nu_i)^{-1}$
1	1	1
2	1.752	0.876
4	3.211	0.803
8	6.041	0.755
16	11.532	0.721

The following list direct costs (in 1997 $) for all of the multi-unit plant systems. Costs for one unit displayed.

<u>Driver group</u>

Driver $\qquad C_{dNe}(Ed) := 116.53\cdot Ed + 140.5$

$$C_{dNe}\left[\left(Ec_{mo_9} + Ei_{2d_9}\right)\cdot 10^{-3}\right] = 163 \quad \text{($M)}$$

Driver cooling and power vs RR $\qquad C_{dRR}(Ed, RR, Nu) := 67\cdot\left(\frac{Nu\cdot RR\cdot Ed\cdot 0.35}{20\cdot\eta_d(Ed, 1, \tau a, 0.22)}\right)^{0.67}$

$$C_{dRR}\left[\left(Ec_{mo_9} + Ei_{2d_9}\right)\cdot 10^{-3}, RRc_9, 1\right] = 23 \quad \text{($M), one unit}$$

Beam switchyard $\qquad CBSY(Nu) := 25\cdot(cd(Nu) - 1)$ ($M), one unit

Target injector system $C_{INJ}(RR, Nu) := 5.7 \cdot \left(RR \cdot 5^{-1}\right)^{0.7} \cdot cd(Nu)$

$C_{INJ}\left(RRc_9, 1\right) = 12$ ($M), one unit

Driver building $C_{DRB}(Ed) := 33.4 \cdot \left(Ed \cdot 4^{-1}\right)^{0.5}$

$C_{DRB}\left[\left(Ec_{mo_9} + Ei_{2d_9}\right) \cdot 10^{-3}\right] = 7.3$ ($M), one unit

Subtotal, driver group cost

$C_{DRG}(Ed, RR, Nu) := C_{dNe}(Ed) + C_{dRR}(Ed, RR, Nu) + C_{INJ}(RR, Nu) + C_{DRB}(Ed)$

$C_{DRG}\left[\left(Ec_{mo_9} + Ei_{2d_9}\right) \cdot 10^{-3}, RRc_9, 1\right] = 206$ ($M), one chamber unit

Fusion chamber group

Fusion chamber $C_{FC}(Pt, Y, Nu) := 17.2 \cdot \left[\left(Pt \cdot 2500^{-1}\right)^{0.855} + Y \cdot 350^{-1}\right] \cdot cd(Nu)$

$C_{FC}\left(Pth_9, Y_{2d_9}, 1\right) = 8.2$ ($M), one unit

Fusion chamber buildings $C_{FCB}(Pt, \eta, Nu) := 30.9 \cdot 1.06 \cdot \left(Pt \cdot \eta \cdot 1100^{-1}\right) \cdot cd(Nu)$

$C_{FCB}\left(Pth_9, \eta_{spp}, 1\right) = 9.5$ ($M), one unit

Bypass pumps $C_{BPP}(RR, Rc, Nu) := 65.7 \cdot \left(RR \cdot 6^{-1}\right)^2 \cdot \left(Rc \cdot 3.5^{-1}\right)^3 \cdot cd(Nu)$

$C_{BPP}\left(RRc_9, Rcbr_9, 1\right) = 27$ ($M), one unit

Bypass pipes $C_{BPPipes}(Pt, Nu) := 11 \cdot \left(Pt \cdot 2500^{-1}\right)^{0.69} \cdot cd(Nu)$

$C_{BPPipes}\left(Pth_9, 1\right) = 4.8$ ($M), one unit

Flibe coolant $C_{Flibe}(Pt, Nu) := 50 \cdot 10^{-6} \cdot 1.06 \cdot 1.22 \cdot 1.936^{-1} \cdot 1970 \cdot \left(1202 \cdot Pt \cdot 2500^{-1}\right) \cdot cd(Nu)$

$C_{Flibe}\left(Pth_9, 1\right) = 23.4$ ($M), one unit

Target factory (Woodworth / Meier model)

$C_{TFE}(RR, Pt, \eta, Nu) := 56 \cdot \left[0.14 + 0.73 \cdot \left(RR \cdot Nu \cdot 5^{-1}\right)^{0.7} + 0.13 \cdot \left(Nu \cdot Pt \cdot \eta \cdot 1000^{-1}\right)^{0.67}\right]$

$C_{TFE}\left(RRc_9, Pth_9, \eta_{spp}, 1\right) = 98$ ($M)

Target factory building $C_{TFB}(RR, Nu) := 15.8 \cdot \left(RR \cdot Nu \cdot 5^{-1}\right)^{0.3}$

$C_{TFB}\left(RRc_9, 1\right) = 21.8$ ($M)

Tritium management system $C_{TMS}(Pt, Nu) := 110 \cdot \left(Pt \cdot 2500^{-1}\right)^{0.7} \cdot cd(Nu)$

$C_{TMS}\left(Pth_9, 1\right) = 46.9$ ($M), one unit

Heat transport system (Coolant loop piping, coolant valves, bellows, pumps, motors, cleanup, steam separators and steam generators, water loop piping)

$$C_{HTS}(Pt,Nu) := 192\cdot\left(Pt\cdot 2500^{-1}\right)^{0.6}\cdot cd(Nu)$$

$$C_{HTS}\left(Pth_9,1\right) = 93 \qquad (\$M), \text{ one unit.}$$

Remote maintenance equipment

$$C_{RME}(Pt,\eta,Nu) := 48\cdot\left(Pt\cdot\eta\cdot 1000^{-1}\right)^{0.6} + 11.9\cdot\left(Pt\cdot\eta\cdot 1000^{-1}\right)^{0.6}\cdot cd(Nu)$$

$$C_{RME}\left(Pth_9,\eta_{spp},1\right) = 30.1 \quad (\$M), \text{ one unit}$$

Subtotal, fusion chamber group cost

$$\begin{aligned} C_{FCG}(RR,Pt,\eta,Rc,Y,Nu) := {} & C_{FC}(Pt,Y,Nu) + C_{FCB}(Pt,\eta,Nu) + C_{BPP}(RR,Rc,Nu) \ldots \\ & + C_{BPPipes}(Pt,Nu) + C_{Flibe}(Pt,Nu) + C_{TFE}(RR,Pt,\eta,Nu) \ldots \\ & + C_{TFB}(RR,Nu) + C_{TMS}(Pt,Nu) + C_{HTS}(Pt,Nu) \ldots \\ & + C_{RME}(Pt,\eta,Nu) \end{aligned}$$

$$C_{FCG}\left(RRc_9,Pth_9,\eta_{spp},Rcbr_9,Y_{2d_9},1\right) = 362 \qquad (\$M), \text{ one unit.}$$

Steam power plant group

Land and land rights

$$C_{LLR}(Nu) := 13.1\cdot cd(Nu)$$

$$C_{LLR}(1) = 13.1 \qquad (\$M), \text{ one unit}$$

Steam plant buildings

$$C_{SPB}(Pt,\eta,Nu) := 85.5\cdot\left(Pt\cdot\eta\cdot 1100^{-1}\right)^{0.5}\cdot cd(Nu)$$

$$C_{SPB}\left(Pth_9,\eta_{spp},1\right) = 46 \qquad (\$M), \text{ one unit}$$

Turbine plant equipment

$$C_{TPE}(Pt,\eta,Nu) := 244\cdot\left(Pt\cdot\eta\cdot 1282^{-1}\right)^{0.8}\cdot cd(Nu)$$

$$C_{TPE}\left(Pth_9,\eta_{spp},1\right) = 80.1 \qquad (\$M), \text{ one unit}$$

Electrical plant equipment

$$C_{EPE}(Pt,\eta,Nu) := 78\cdot\left(Pt\cdot\eta\cdot 1282^{-1}\right)^{0.4}\cdot cd(Nu)$$

$$C_{EPE}\left(Pth_9,\eta_{spp},1\right) = 44.7 \qquad (\$M), \text{ one unit}$$

Miscellaneous plant equipment

$$C_{MPE}(Pt,\eta,Nu) := 30\cdot\left(Pt\cdot\eta\cdot 1282^{-1}\right)^{0.3}\cdot cd(Nu)$$

$$C_{MPE}\left(Pth_9,\eta_{spp},1\right) = 19.8 \qquad (\$M), \text{ one unit}$$

Heat rejection equipment

$$C_{HRE}(Pt,\eta,Nu) := 30\cdot\left[Pt\cdot(1-\eta)\cdot 1719^{-1}\right]^{0.8}\cdot cd(Nu)$$

$$C_{HRE}\left(Pth_9,\eta_{spp},1\right) = 9.8 \qquad (\$M), \text{ one unit}$$

Subtotal, steam power plant group cost

$$C_{SPG}(Pt,\eta,Nu) := C_{LLR}(Nu) + C_{SPB}(Pt,\eta,Nu) + C_{TPE}(Pt,\eta,Nu) \ldots + C_{EPE}(Pt,\eta,Nu) + C_{MPE}(Pt,\eta,Nu) + C_{HRE}(Pt,\eta,Nu)$$

$C_{SPG}(Pth_9,\eta_{spp},1) = 213.4$ ($M), one unit

Total direct costs $C_T(Ed,RR,Pt,\eta,Rc,Y,Nu) := C_{DRG}(Ed,RR,Nu) \ldots + C_{FCG}(RR,Pt,\eta,Rc,Y,Nu) \ldots + C_{SPG}(Pt,\eta,Nu)$

$C_T\left[\left(Ec_{mo_9} + Ei_{2d_9}\right)\cdot 10^{-3}, RRc_9, Pth_9, \eta_{spp}, Rcbr_9, Y_{2d_9}, 1\right] = 781$ ($M), one unit

Cost of electricity

Annual charges for operations and scheduled component replacements (fraction of total direct costs) $OM\_SCR := 0.03$

Annual charges for target factory $OM_{TF}(RR,Nu) := 13.5\cdot\left(Nu\cdot RR\cdot 5^{-1}\right)^{0.3}$ ($M/yr)

Fixed charge rate $FCR := 0.08$

Indirect cost multiplier $IDC := 1.936$

Plant availability $f_a := 0.85$ (for thick-liquid-protected chambers)

Lithium, deuterium fuel $CoE_{DLi} := 0.0048$ (cts/kWehr)

Decommissioning $CoE_{dec} := 0.12$ (cts/kWehr)

Cost of electricity:

Eq. 39

$$CoE(C_T,Nu,Pnet,RR) := \frac{C_T\cdot(IDC\cdot FCR + OM\_SCR) + OM_{TF}(RR,Nu)}{0.0876\cdot Nu\cdot Pnet\cdot f_a} + CoE_{DLi} + CoE_{dec}$$

cts/kWehr

As a function of the number of units,

$$CoE9_i := CoE\left[C_T\left[\left(Ec_{mo_9} + Ei_{2d_9}\right)\cdot 10^{-3}, RRc_9, Pth_9, \eta_{spp}, Rcbr_9, Y_{2d_9}, Nu_i\right], Nu_i, Pnet_9, RRc_9\right]$$

total direct capital costs $C_{T9_i} := C_T\left[\left(Ec_{mo_9} + Ei_{2d_9}\right)\cdot 10^{-3}, RRc_9, Pth_9, \eta_{spp}, Rcbr_9, Y_{2d_9}, Nu_i\right]$

Substem group direct costs: ($M)

$C_{DRG9_i} := C_{DRG}\left[\left(Ec_{mo_9} + Ei_{2d_9}\right)\cdot 10^{-3}, RRc_9, Nu_i\right]$ Driver group ($M)

$C_{FCG9_i} := C_{FCG}\left(RRc_9, Pth_9, \eta_{spp}, Rcbr_9, Y_{2d_9}, Nu_i\right)$ Fusion chamber group

$C_{SPG9_i} := C_{SPG}\left(Pth_9, \eta_{spp}, Nu_i\right)$ Steam plant group

For comparison, the future price of natural gas (PNG) in dollars per million BTU ~ \$/GJ $_{th}$ at which modular gas turbines with a direct capital cost of 400 \$/kWe and a gas turbine efficiency of 36% (no steam bottoming cycle) would produce the same CoE as projected for this small fusion plant, assuming the same indirect capital cost multiplier, plant availability factor, fixed charge rate and annual operating costs as a percentage of capital, would be given by

$$PNG(CoE) := CoE - 4.56 \cdot \left(\frac{IDC \cdot FCR - OM\_SCR}{f_a} \right) \qquad PNG9_i := PNG\left(CoE9_i\right) \qquad \text{Eq. 40}$$

(\$/MBTU)

Tabel 3 Summary of economics for a modular IFE plant scaleable from a small 290 MWe pilot plant to large multi-chamber plant outputs, based on ion-driven fast ignition of ρr = 2 g/cm^2 targets, as a function of the number of modular chambers sharing a common driver (through a beam switchyard) and common target factory [18].

# of units	Total output	Shared Driver rep-rate	Cost of Electr.	Direct costs, driver group	Direct costs, chamber group	Direct costs, steam BoP group	Total direct costs	Competitive natural gas price for GTs
Nu_i =	$Nu_i \cdot Pnet9$	$Nu_i \cdot RRc9$ =	$CoE9_i$ =	C_{DRG9_i} =	C_{FCG9_i} =	C_{SPG9_i} =	C_{T9_i} =	$PNG9_i$ =
1	290.562	14.594	7.659	205.571	361.997	213.36	780.927	6.989
2	581.124	29.187	5.737	228.503	587.233	373.807	$1.19 \cdot 10^3$	5.067
4	$1.162 \cdot 10^3$	58.375	4.63	268.157	$1.003 \cdot 10^3$	685.073	$1.956 \cdot 10^3$	3.96
8	$2.324 \cdot 10^3$	116.749	3.96	337.39	$1.776 \cdot 10^3$	$1.289 \cdot 10^3$	$3.402 \cdot 10^3$	3.29
16	$4.649 \cdot 10^3$	233.498	3.53	459.459	$3.224 \cdot 10^3$	$2.46 \cdot 10^3$	$6.144 \cdot 10^3$	2.86
	(MWe)	(Hz)	(cts/kWehr)	(\$M)	(\$M)	(\$M)	(\$M)	(\$ / MBTU)

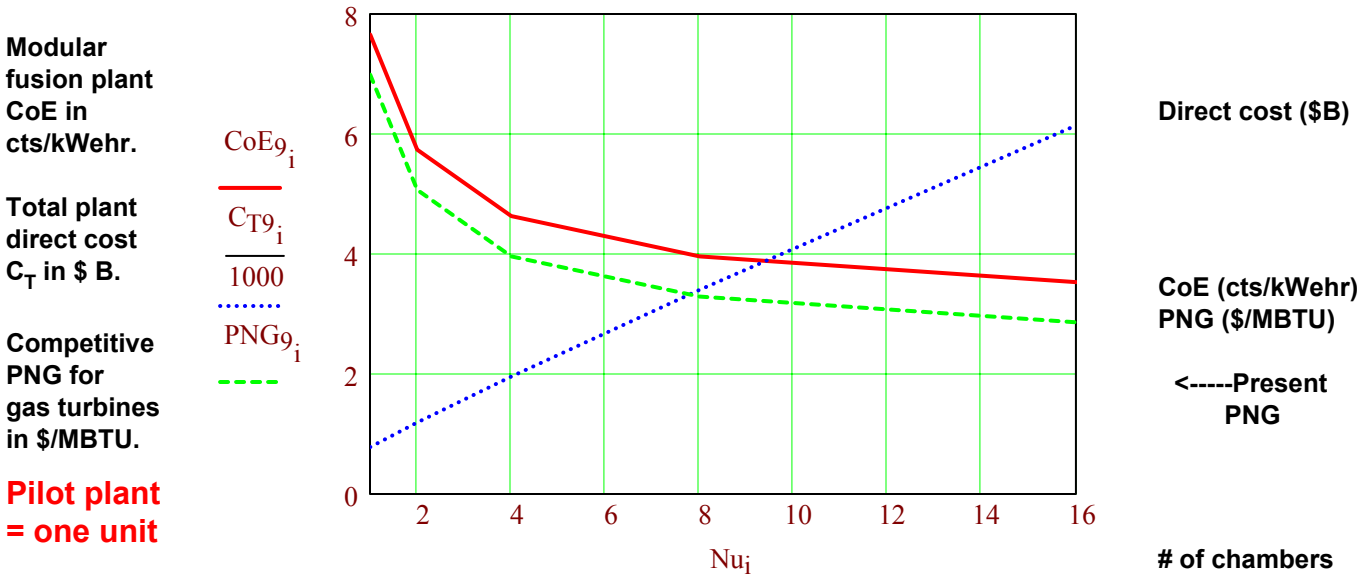

Fig. 11 : CoE (cts/kWehr), total direct capital cost (\$ B), and competitive price of gas (PNG), for modular fusion IFE plants as a function of the number of fusion chambers sharing a common driver and target factory. Steam BoP, small ρr = 2 g/cm^2 (case 9) fast ignition targets.

Electric plants using large fast ignition targets and MHD plasma direct conversion.

Following reference [8], we next consider the possibility of using the large ρr = 10 g/cm^2 targets (case 10) to capture a majority of the fusion neutrons, as well as the alpha particles, for subsequent plasma direct conversion. Instead of stopping the neutrons in an thick external target shell two or more mean-free-paths thick, which required very large fusion yields to ionize in ref. [8], only a few cm-thick target shell is needed because the neutrons are now stopped within the target core itself. The thin target shell, made of potassium or a potassium-containing molten salt, has just enough mass to mix with the target plasma debris to downshift the plasma temperature to a more optimum 2 eV, where conductivity is still high for efficient MHD direct conversion, but where radiation losses to the fusion chamber and MHD channel walls are small compared to the plasma enthalpy flow and conversion rates [8]. In this situation, the usual HYLIFE-II problem of clearing the chamber from jet bulk-liquid breakup due to isochoric neutron heating, is greatly diminished for a given yield. In this case 10, out of a total fusion yield

$$Y_{mo_{10}} = 1084 \qquad \text{(MJ)},$$

only 20 %, or $0.2 \cdot Y_{mo_{10}} = 217$ (MJ), is available for isochoric heating of the molten salt liquid layers used to protect the chamber walls, less than in the original HYLIFE-II chamber design. In this case we use a horizontal vortex such as described in ref. [19], an adaptation of the old BLASCON concept [20] in which the free surface liquid is held "down = radially" with several-g's of effective gravity, and gas bubbles are injected into the outer part of the vortex near the wall to absorb shocks (see Fig. 12). If we also increase the inner liquid surface radius as shown in Fig. 12 to ~ 2.5 meters, 5 times the HYLIFE-II inner liquid radius of ~ 0.5 m, then the isochoric neutron heating deposition in the protective molten-salt is reduced below 10 J/cm^3 (< few degrees C ΔT per pulse), where we can avoid bulk liquid breakup due to isochoric neutron heating entirely. In addition, the use of a few-cm target shell for MHD plasma temperature control also acts as a soft-x-ray debris shield, with the result that there is little or no molten salt vaporization or splash created by the 1000 MJ yield of the large target.

The resulting dense target + shell plasma (with a sound velocity ~ 8000 m/s) fills the ~ 100 m^3 vortex open volume to about 20 to 40 bar each shot, and escapes preferentially to the right in Fig. 12 through ~ 1 m^2 MHD generator channel shown opening, in a characteristic exhaust time of ~ 20 ms. A strong solenoidal field peak on the beam and target injection side aids in focusing the ion beams, and also greatly restricts the plasma flow toward the beam entrances. A relatively weak guide magnetic field in the vortex center would also help damp the plasma turbulence, and promote more uniform flow into the MHD channel. Without liquid break-up, there would be no substantial mixing of the plasma with the molten-salt vortex layer that protects the walls. (About 1-3 kg of vaporized or mixed-in molten salt droplets could still be tolerated each shot, where the salt just becomes part of the MHD plasma working fluid in the cycle). In this case, the chamber pulse rate is not limited by clearing of relatively-slow-moving liquid, but by the target + shell plasma exhaust time out the MHD channel at much higher plasma sound velocity. This means that such a chamber could have a pulse rate of 20 Hz or more. Because of the high pulse rate, the MHD generation would occur over a substantial duty factor despite the low pressure recovery before each target is injected (no need to inject under high plasma pressure as was assumed in ref. [8].

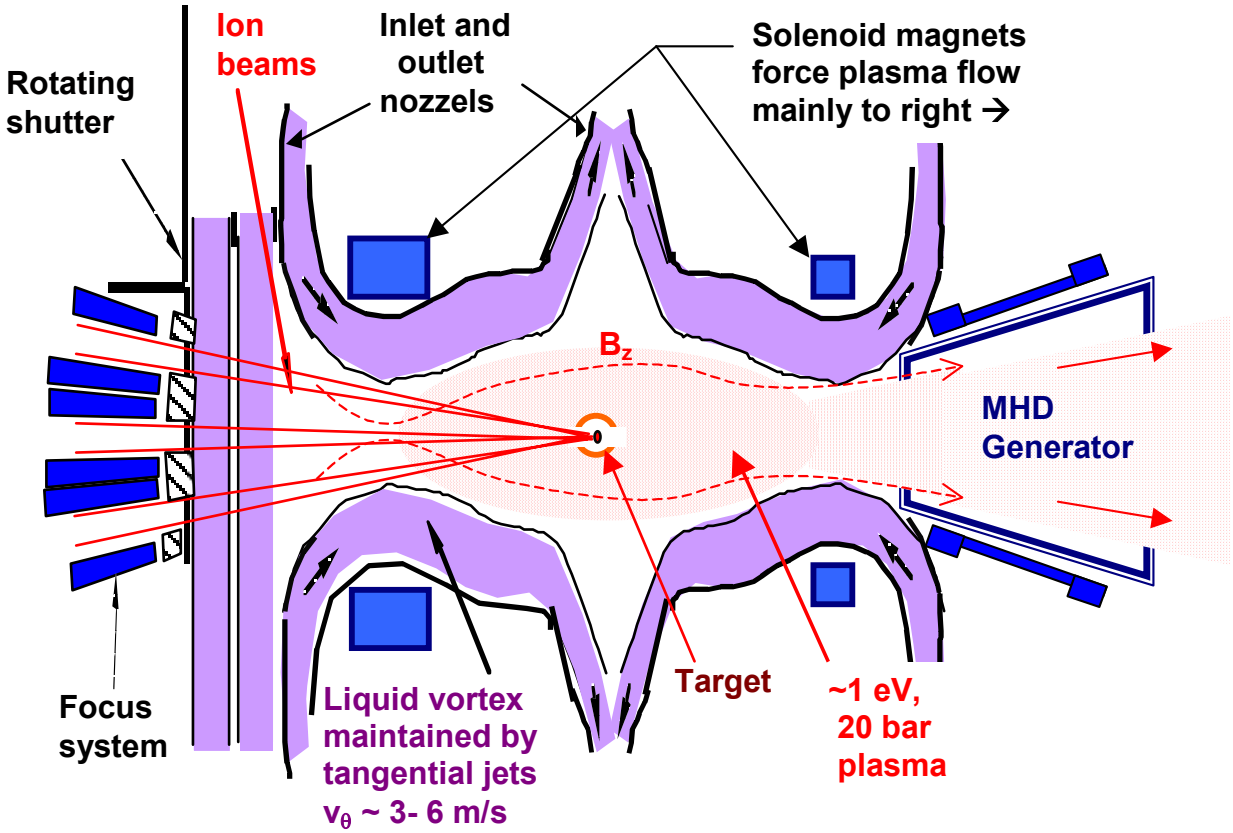

Fig. 12 : A conceptual fusion chamber with MHD plasma direct conversion for ion fast ignition with large ρr = 10 g/cm^2 targets (case 10). Tangential jets create enough atificial gravity to prevent liquid breakup due to isochoric neutron heating, with ~ 100 m^3 open vortex volume at R_{vortex} ~ 2.5 m, and fusion neutron yield (escaping to the walls) ~ 200 MJ out of ~ 1 GJ total fusion yield. Since the targets are tritium lean and self-breed, the choice of molten salt can dispense with the need for either lithium or beryllium. The ion beam focusing system takes into account the solenoid field, also used to direct the plasma flow preferrentially into the MHD generator on the right. MHD generator efficiency ~ 33% expected (ref. [8]). Plasma sound speeds (~8000m/s) are high enough to recover the chamber to low pressures before target injection within ~ 20 to 50 ms. A steam bottoming cycle may optionally be used to achieve a higher combined cycle efficiency of 62 %.

We now estimate the economics of the large power plant case with a combined MHD + steam cycle efficiency of

$$\eta_{MHDs} := 0.62$$

We take case 10 large targets, in a single chamber as shown in Fig. 12, with variable pulse repetition rates of

$$RRc10_i := 2^i \quad \text{Hz.}$$

The associated driver recirculating powers are

$$Pde10_i := \left(Ec_{mo_{10}} + Ei_{mo_{10}}\right)\cdot 10^{-3}\cdot\left(\eta d_{10}\right)^{-1}\cdot RRc10_i$$

The associated fusion chamber average themal powers and net electric outputs are

$$Pth10_i := Y_{mo_{10}}\cdot RRc10_i \quad \text{(MWth), and}$$

$$Pnet10_i := Pth10_i\cdot\eta_{MHDs}\cdot\left(1 - f_{aux}\right) - Pde10_i \quad \text{(MWe), respectively.}$$

$RRc10_i =$	$Pth10_i\cdot 10^{-3} =$	$Pde10_i =$	$Pnet10_i\cdot 10^{-3} =$
2	2.168	13.373	1.264
4	4.336	26.746	2.527
8	8.672	53.492	5.054
16	17.343	106.985	10.108
32	34.686	213.97	20.216
(Hz)	(GWth)	(MWe)	(GWe)

The highest pulse rates andpower levels would be appropriate for hydrogen production for transportation fuel on a scale commensurate with modern oil refineries [18]. To illustrate the potential benefits of such large fast ignition targets using direct conversion, we will simply modify appropriate HYLIFE-II chamber and steam BoP subsystem descriptions, efficiencies and costs from refs. [17] and 18] which we used in the previous modular small power plant examples, by applying appropriate cost multipliers to each subsystem for the case of MHD conversion, using guidance from ref. [8] where appropriate. In doing so, we will also credit the appropriate costs savings in target fabrication, molten salt costs and handling, and tritium management since the large case 10 targets are self-breeding. Assuming a combined cycle with MHD BoP cost of $240/kWe (twice the value estimated in ref. [8]), and a steam BoP cost of $ 730 /kWe, the effective BoP cost reduction factors, weighted in terms of the amounts of electricity recovered from each part of the combined cycle, would be

$$F_{MHDS} := \frac{240\cdot 0.33 + 730\cdot(1 - 0.33)\cdot\eta_{spp}}{730} \qquad F_{MHDS} = 0.4$$

Driver group, large targets with MHD

$$C_{DRG10_i} := C_{DRG}\left[\left(Ec_{mo_{10}} + Ei_{mo_{10}}\right)\cdot 10^{-3}, RRc_{10_i}, 1\right] \qquad (\$M), \text{ one unit}$$

Fusion chamber group modified for vortex chambers, large targets, no T-breeding, and MHD

$$\begin{aligned} C_{FCG10}(RR, Pt, \eta, Rc, Y, Nu) := {} & C_{FC}(Pt, Y, Nu) + C_{FCB}(Pt, \eta, Nu) + \frac{C_{BPP}(RR, Rc, Nu)}{10} \ldots \\ & + \frac{C_{BPPipes}(Pt, Nu)}{10} + \frac{C_{Flibe}(Pt, Nu)}{3} + C_{TFE}(RR, Pt, \eta, Nu) \ldots \\ & + C_{TFB}(RR, Nu) + \frac{C_{TMS}(Pt, Nu)}{3} + C_{HTS}(Pt, Nu) \ldots \\ & + C_{RME}(Pt, \eta, Nu) \end{aligned}$$

Note we reduced the molten-salt pumping costs, because the vortex needs far less pump power to maintain than does HYLIFE-II, we reduced the Flibe costs to credit the possibility of using a mothen salt without beryllium, and we reduced the tritium management system, (as T-breeding is not longer required).

$$C_{FCG10_i} := C_{FCG10}\left(RRc_{10_i}, Pth_{10_i}, \eta_{MHDs}, 3.5, Y_{mo_{10}}, 1\right) \qquad (\$M), \text{ one unit}$$

Energy conversion BoP with MHD

$$C_{SPG10_i} := F_{MHDS}\cdot C_{SPG}\left(Pth_{10_i}, \eta_{MHDs}, 1\right) \qquad (\$M), \text{ one unit}$$

Total direct costs (Large targets with MHD)

$$C_{T10_i} := C_{DRG10_i} + C_{FCG10_i} + C_{SPG10_i} \qquad (\$M), \text{ one unit}$$

Cost of Electricity (Large targets with MHD)

$$CoE_{10_i} := CoE\left(C_{T10_i}, 1, Pnet_{10_i}, RRc_{10_i}\right) \qquad (cts/kWehr)$$

Competitive price of natural gas for same CoE with gas turbines

$$PNG_{10_i} := PNG\left(CoE_{10_i}\right) \qquad (\$/MBTU)$$

Table 4 **Economics for an advanced IFE plant with combined cycle MHD [8] and steam energy conversion BoP, based on ion-driven fast ignition of large ρr = 10 g/cm² targets with tritium-lean (self-breeding) targets. 4 MJ driver, 1 GJ yield. Power vs pulse rate.**

Rep-rate	Total output $\frac{Pnet10_i}{10^3}$ =	Cost of Electr.	Direct costs, driver group	Direct costs, chamber group	Direct costs, MHD/ steam BoP group	Total direct costs	Competitive natural gas price for GTs
$RRc10_i$ =		$CoE10_i$ =	$C_{DRG}10_i$ =	$C_{FCG}10_i$ =	$C_{SPG}10_i$ =	$C_{T}10_i$ =	$PNG10_i$ =
2	1.264	2.865	681.419	464.323	193.376	$1.339 \cdot 10^3$	2.195
4	2.527	1.874	698.26	712.298	301.14	$1.712 \cdot 10^3$	1.204
8	5.054	1.313	725.119	$1.131 \cdot 10^3$	478.023	$2.334 \cdot 10^3$	0.643
16	10.108	0.985	767.953	$1.861 \cdot 10^3$	771.463	$3.4 \cdot 10^3$	0.315
32	20.216	0.791	836.272	$3.197 \cdot 10^3$	$1.263 \cdot 10^3$	$5.296 \cdot 10^3$	0.121
(Hz)	(GWe)	(cts/kWehr)	($M)	($M)	($M)	($M)	($ / MBTU)

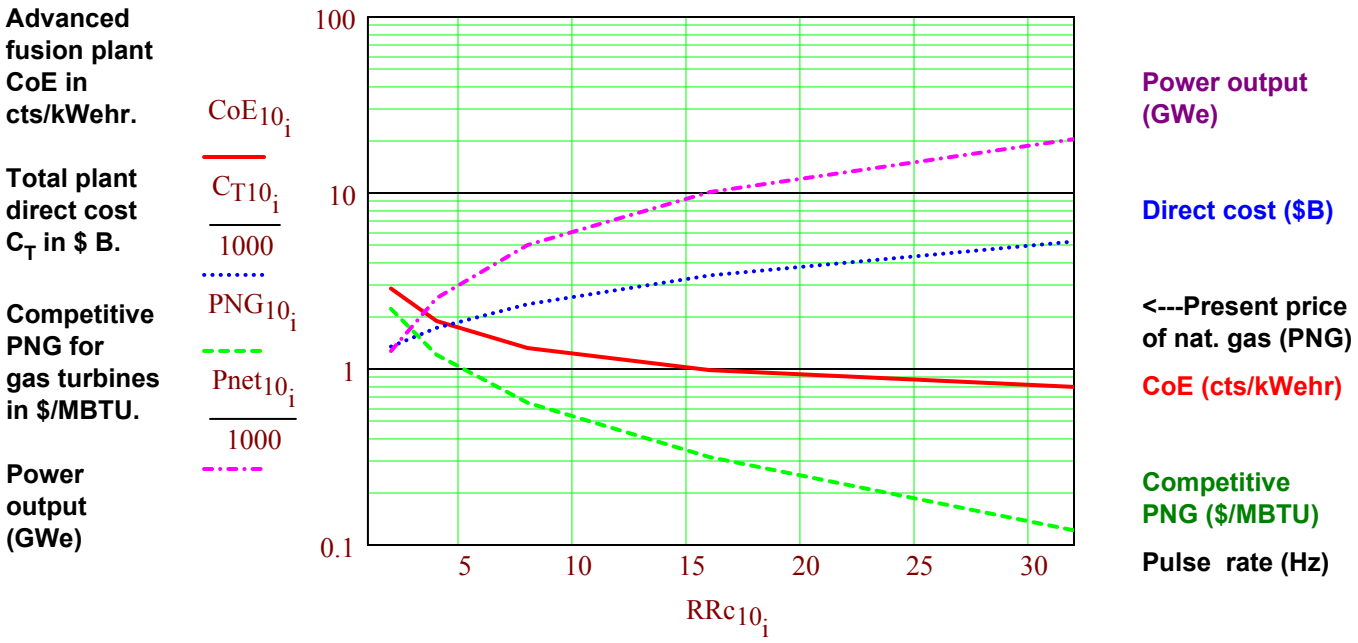

Fig. 13 : CoE (cts/kWehr), total direct capital cost ($ B), and competitive price of gas (PNG), for a large IFE plant with ion-fast ignition and an advanced MHD+steam balance of plant, as a function of the fusion chamber pulse rate (Hz). Large ρr = 10 g/cm² (case 10) targets. Key reference [8]: Logan, "Inertial fusion reactors using Compact Fusion Advanced Rankine (CFARII) MHD conversion", Fusion Engineering and Design 22 (1993), p. 151

Acknowledgements

We wish to acknowledge useful discussions with H. Kirbie and S. Sampayan (LLNL) on short-pulse accelerator and switching approaches , with John Barnard (LLNL) on some beam physics formulations, with K. Nishihara and T. Azechi (ILE, Osaka University) on ways to increase minimum pulse lengths for ion fast ignition, and with D. Hoffmann, A. Tauschwitz, and M. Roth (GSI, Germany), on adaptation of plasma lens for ion fast ignitor beam experiments.

References:

[1] M. Tabak, et. al., Phys. Plasmas 1, 1626, 1994
[2] Tabak/Callahan's distributed radiator target designs (to be published).
[3] R. Stevens, et. al., "Laser fast ignition: an attractive approach to inertial fusion energy". (in these proceedings)
[4] A. Maschke, "Initiation of Thermonuclear Detonations", Brookhaven National Laboratory report BNL 19008, EP&S-3, June 5, 1974
[5] S. Atzehni, Heidelberg HIF-97 paper.
[6] A. Faltens (LBNL) private communication (Nov. 1997).
[7] G. Caporaso, "The Dielectric Wall Accelerator", in Frontiers of Accelerator Technology, (Kurokawa, et. al., Editors), pgs 607-615, World Scientific Publishing Ltd., Copywrite 1996
[8] G. Logan, "Compact Fusion Advanced Rankine Cycle", Fusion Engineering and Design
[9] P. Thieberger, et. al., "Fully-stripped heavy-ion yield vs energy for Xe and Au ions", Transactions on Nuclear Science, Vol. NS-32, No. 5, p. 1767, October 1985
[10] D. Callahan and G. Logan, Heidelberg paper on "Charge and current neutralization of high-charge-state ions". Sept. 1997
[11] GSI plasma lens reference
[12] Rod Mason (LANL) reference for ANTHEM code.
[13] H. Daido, et.al., "Generation of a strong magnetic field by an intense CO2 laser pulse". Phys. Rev. Letters, 56, No. 8, p. 846 (Feb., 1986)
[14] Ralph Page (LLNL) Zinc-Selenide DPSSL reference
[15] R. Bangerter, et. al -Nuclear Fusion article on heavy-ion-plasma interaction near targets
[16] W. Meier, et. al. Heidelberg HIF Symposium paper on integrated systems model for a heavy-ion driver, Sept. 1997.
[17] R. Moir, et. al., HYLIFE-II.
[18] G. Logan, et. al., Fusion Tech. Vol. 28, p.1674 (Nov. 1995).